 CMES, vol.52, no.1, pp.1-37, 2009

A DRK Interpolation-Based Collocation Method for the Analysis of Functionally Graded Piezoelectric Hollow Cylinders under Electro-Mechanical Loads

Chih-Ping Wu[1,2], Jian-Sin Wang[2] and Yung-Ming Wang[2]

Abstract: A meshless collocation method based on the differential reproducing kernel (DRK) interpolation is developed for the three-dimensional (3D) coupled analysis of simply-supported, functionally graded (FG) piezoelectric hollow cylinders. The material properties of FG hollow cylinders are regarded as heterogeneous through the thickness coordinate, and then specified to obey an exponent-law dependent on this. In the present formulation, the shape function for the reproducing kernel (RK) interpolation function at each sampling node is separated into a primitive function possessing Kronecker delta properties and an enrichment function constituting reproducing conditions. By means of this DRK interpolation, the essential boundary conditions can be readily applied, exactly like the implementation in the finite element method (FEM). An additional innovation of this meshless method is that the shape functions for derivatives of the RK interpolation functions are determined using a set of differential reproducing conditions, rather than directly differentiating them. In the implementation of the DRK interpolation-based collocation method presented in this work, some crucial parameters are discussed, such as the optimal support size and the highest-order of the basis functions. The influence of the material-property gradient index on the field variables induced in the FG hollow cylinders is also studied.

Keywords: DRK interpolation, Collocation methods, Meshless methods, Coupled piezoelectric effects, FG material, Cylinders.

1 Introduction

In recent decades, functionally graded (FG) piezoelectric structures have been widely used in various engineering applications for sensing, actuating and controlling purposes due to their direct and converse multi-field effects. The material properties

[1] Corresponding author. Fax: +886-6-2370804, E-mail: cpwu@mail.ncku.edu.tw
[2] Department of Civil Engineering, National Cheng Kung University, Tainan 70101, Taiwan, ROC

of these FG structures are designed to gradually and continuously vary through the thickness coordinate. This feature is helpful in preventing from some drawbacks that often occur in multilayered structures, such as residual stress concentration induced in a high temperature environment and large inter-laminar stresses induced at interfaces between adjacent layers. However, this feature also increases the complexity and difficulty of the analysis of these FG structures. Consequently, far fewer published articles deal with the mechanical problems of FG structures in comparison to those that consider multilayered structures.

The published three-dimensional (3D) analytical methods for the analysis of multilayered and FG piezoelectric shells and plates were classified into four different approaches, namely the Pagano, state space, series expansion and asymptotic approaches by Wu, Chiu and Wang (2008a). The 3D static behaviors of multilayered piezoelectric cylinders and plates were studied by Heyliger (1997a, b) using the Pagano approach, which was also applied to the cylindrical bending deformation and vibration analyses of multilayered plates by Heyliger and Brooks (1995, 1996). A modified Pagano approach was developed for the coupled analysis of FG magneto-electro-elastic plates (Wu and Lu, 2009; Wu and Chen, 2009). Zhong and Shang (2003, 2005) and Wu and Liu (2007) presented the 3D exact analyses of FG piezoelectric and piezo-thermo-elastic plates using the state space approach in conjunction with the transfer matrix method. Based on the series expansion method, Kapuria, Sengupta and Dumir (1997a) presented the 3D exact solutions for the coupled electro-elastic analysis of single-layer homogeneous piezoelectric cylindrical hollow cylinders under axisymmetric loads, while Kapuria, Sengupta and Dumir (1997b) and Kapuria, Dumir and Sengupta (1997) presented the 3D piezo-thermo-elastic analysis of multilayered hollow cylinders under axisymmetric and nonaxisymmetric thermo-electric loads, respectively. An asymptotic approach was developed for a variety of mechanical problems of simply-supported, multilayered and FG shells made up of smart materials (Wu and Chi, 2004; Wu, Lo and Chao, 2005; Wu and Lo, 2006; Wu, Syu and Lo, 2007; Wu and Syu, 2006, 2007; Wu and Tsai, 2009). More details about the developments, ideas and applications of these earlier analytical approaches can be found in Wu, Chiu and Wang (2008a).

In addition to the earlier 3D analytical approaches, some approximate 3D numerical modeling methodologies have also been proposed for the coupled analysis of multilayered and FG piezoelectric shells and plates. Ramirez, Heyliger and Pan (2006a, b) proposed a discrete layer approach in combination with the Ritz method (or the finite element method, FEM) to investigate the static and free vibration responses of FG material plates. The discrete layer scheme was demonstrated to be not limited to specific boundary conditions and gradation functions. Cheung and Jiang (2001) and Akhras and Li (2007) studied the 3D static and 3D static, vibra-

tion and stability analyses of piezoelectric plates, respectively, using a finite layer method.

In recent decades, meshless methods in which the relevant approximate or interpolate functions are constructed using the random distribution of nodes have attracted the considerable attention. These approaches include the diffuse element method (Nayroles, Touzot and Villon, 1992), the element-free Galerkin method (Belytschko, Lu and Gu, 1994), the moving least squares method (Lancaster and Salkauakas, 1981), the meshless local Petrov-Galerkin (MLPG) method (Atluri and Zhu, 1998, 2000; Atluri, Han and Shen, 2003) and the reproducing kernel particle method (Liu, Jun and Zhang, 1995). It has been reported that the drawbacks of FEM in treating discontinuity, moving boundary and large deformation problems can be overcome. However, it is noted that in the earlier Galerkin-based meshless methods, except for the MLPG method, a background mesh is still needed to evaluate the integral of weak formulation. Based on the MLPG method, which is truly meshless, Atluri and Shen (2002a) made a comparison study of the efficiency and accuracy of a variety of meshless trial and test functions. Through a mixed MLPG approach, Atluri, Han and Rajendran (2004) presented a new implementation of the meshless finite volume method for the analysis of elasto-static problems. Comprehensive literature surveys of meshless methods were undertaken by Atluri (2004), Atluri and Shen (2002b), Belytschko, Krongauz and Organ (1996) and Liu (2003).

Apart from the earlier Galerkin-based meshless methods, some collocation-based approaches using different types of approximate or interpolate functions have been developed for solving the strong formulation of elastic solids (or fluids) in the literature. A point collocation method based on the reproducing kernel (RK) approximation has been proposed by Aluru (2000) for numerical solution of partial differential equations with appropriate boundary conditions. The method has been shown to be accurate for some one- and two-dimensional problems of elastic solids. Oñate et al. (1996) presented a finite point method based on the weighted least squares interpolation for the analysis of convective-diffusive transport and compressible fluid flow problems. Sladek et al. (2006, 2007) studied the plane piezoelectricity and thermopiezoelectricity using the MLPG method, which was also applied to the transient heat conduction in 3D anisotropic FG solids (Sladek et al., 2008) and the stress and crack analysis in 3D axisymmetric FG material bodies (Sladek et al., 2005).

Recently, a meshless collocation method based on the differential reproducing kernel (DRK) approximation has been developed and applied to the analysis of multilayered and FG piezoelectric and magneto-electro-elastic shells and plates by Wu Chiu and Wang (2008b, c). The novelty of this DRK approximation-based method is in its modifications for calculating derivatives of the RK approximants. In the standard RK method, the shape functions for derivatives of the RK approximants

are obtained by directly differentiating the RK approximants; whereas, in the DRK approximation-based collocation method, they are obtained using a set of differential reproducing conditions, which simplifies the relevant computations.

In this paper, a meshless collocation method based on the DRK interpolation is presented. Unlike the earlier RK and DRK approximations, in which the shape functions of RK approximants do not possess the Kronecker delta properties, those in this DRK interpolation do by means of separating each shape function of the RK function into a primitive function possessing the Kronecker delta properties and an enrichment function constituting the reproducing conditions. The essential boundary conditions can thus be readily applied, exactly like the implementation in the finite element method. A meshless DRK interpolation-based collocation method is developed and applied to the analysis of FG piezoelectric hollow cylinders with open-circuit and closed-circuit surface conditions and under a variety of electro-mechanical loads. A parametric study for the effect of the material-property gradient on the static behavior of the FG piezoelectric hollow cylinders is also undertaken.

2 Basic equations of 3D piezoelectricity

A simply-supported, FG piezoelectric circular hollow cylinder with open-circuit and closed-circuit surface conditions and subject to electro-mechanical loads is considered. The configuration and coordinates of the cylinder are shown in Fig. 1. The material properties are regarded as heterogeneous through the thickness coordinate. A set of the orthogonal curvilinear coordinates (α, β, ζ) is located on the middle surface of the hollow cylinder. The total thickness, length and radius of the cylinder are $2h$, L and R, respectively. In addition, $x_3 = R + \zeta$, in which ζ is the distance measured from the mid-surface of the cylinder in the thickness direction.

The linear constitutive equations valid for the nature of the symmetry class of the piezoelectric material considered are given by

$$\sigma_i = c_{ij}\varepsilon_j - e_{ki}E_k, \tag{1}$$

$$D_l = e_{lj}\varepsilon_j + \eta_{lk}E_k, \tag{2}$$

where σ_i and ε_j (i, j=1–6) are the contracted notation for the stress and strain components, respectively; D_l (l=1–3) and E_k(k=1–3) denote the electric displacement components and the electric field components, respectively; c_{ij}, e_{ki} and η_{lk} are the elastic, piezoelectric and dielectric permeability coefficients, respectively. These material properties are considered as heterogeneous through the thickness coordinate (i.e., $c_{ij}(x_3)$, $\eta_{lk}(x_3)$ and $e_{ki}(x_3)$). For an orthotropic solid, the previous material coefficients are given by

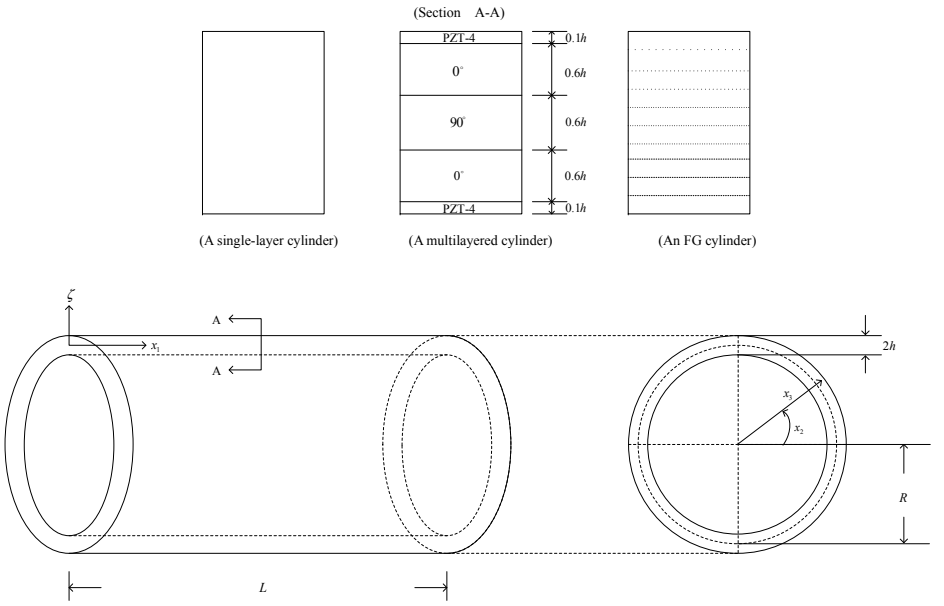

Figure 1: The geometry and coordinates of a hollow cylinder.

$$\mathbf{c}=\begin{bmatrix} c_{11} & c_{12} & c_{13} & 0 & 0 & 0 \\ c_{12} & c_{22} & c_{23} & 0 & 0 & 0 \\ c_{13} & c_{23} & c_{33} & 0 & 0 & 0 \\ 0 & 0 & 0 & c_{44} & 0 & 0 \\ 0 & 0 & 0 & 0 & c_{55} & 0 \\ 0 & 0 & 0 & 0 & 0 & c_{66} \end{bmatrix}, \quad \mathbf{e}=\begin{bmatrix} 0 & 0 & e_{31} \\ 0 & 0 & e_{32} \\ 0 & 0 & e_{33} \\ 0 & e_{24} & 0 \\ e_{15} & 0 & 0 \\ 0 & 0 & 0 \end{bmatrix} \quad \boldsymbol{\eta}=\begin{bmatrix} \eta_{11} & 0 & 0 \\ 0 & \eta_{22} & 0 \\ 0 & 0 & \eta_{33} \end{bmatrix}.$$

The strain-displacement relationships are

$$\begin{Bmatrix} \varepsilon_1 \\ \varepsilon_2 \\ \varepsilon_3 \\ \gamma_{23} \\ \gamma_{13} \\ \gamma_{12} \end{Bmatrix} = \begin{bmatrix} \partial_1 & 0 & 0 \\ 0 & (1/x_3)\,\partial_2 & (1/x_3) \\ 0 & 0 & \partial_3 \\ 0 & \partial_3-(1/x_3) & (1/x_3)\,\partial_2 \\ \partial_3 & 0 & \partial_1 \\ (1/\gamma)\,\partial_2 & \partial_1 & 0 \end{bmatrix} \begin{Bmatrix} u_1 \\ u_2 \\ u_3 \end{Bmatrix}, \tag{3}$$

in which $\partial_i = \partial/\partial x_i$; u_1, u_2 and u_3 are the displacement components.
The stress equilibrium equations without body forces are given by

$$x_3\sigma_{1,1}+\tau_{12,2}+(x_3\tau_{13})_{,3}=0, \tag{4}$$

$$x_3\tau_{12,1}+\sigma_{2,2}+(1/x_3)\left(x_3^2\tau_{23}\right),_3=0, \tag{5}$$

$$x_3\tau_{13,1}+\tau_{23,2}+(x_3\sigma_3),_3-\sigma_2=0. \tag{6}$$

The equation of electrostatics for the piezoelectric material without the electric charge density is

$$x_3D_{1,1}+D_{2,2}+(x_3D_3),_3=0. \tag{7}$$

The relations between the electric field and electric potential are

$$E_k=-\Phi,_k/g_k \quad (k=1,2,3), \tag{8}$$

where Φ denotes the electric potential; and g_k (k=1, 2, 3) are the scale factors of the cylindrical coordinate system, in which $g_1=g_3=1$ and $g_2=x_3$.

Four different lateral surface conditions are considered, as follows:

Case 1. In the cases of closed-circuit and prescribed mechanical load surface conditions,

$$\tau_{13}=\tau_{23}=\Phi=0 \quad \text{on} \quad \zeta=\pm h; \tag{9a}$$

and $\sigma_3=\bar{q}_3^+$ on $\zeta=h$,

$$\sigma_3=0 \quad \text{on} \quad \zeta=-h. \tag{9b}$$

Case 2. In the cases of closed-circuit and prescribed electric potential surface conditions,

$$\tau_{13}=\tau_{23}=\sigma_3=0 \quad \text{on} \quad \zeta=\pm h; \tag{10a}$$

and $\Phi=\bar{\Phi}^+$ on $\zeta=h$,

$$\Phi=0 \quad \text{on} \quad \zeta=-h. \tag{10b}$$

Case 3. In the cases of open-circuit and prescribed mechanical load surface conditions,

$$\tau_{13}=\tau_{23}=D_3=0 \quad \text{on} \quad \zeta=\pm h; \tag{11a}$$

and $\sigma_3=\bar{q}_3^+$ on $\zeta=h$,

$$\sigma_3=0 \quad \text{on} \quad \zeta=-h. \tag{11b}$$

Case 4. In the cases of open-circuit and prescribed electric displacement surface conditions,

$$\tau_{13} = \tau_{23} = \sigma_3 = 0 \quad \text{on} \quad \zeta = \pm h; \tag{12a}$$

and $D_3 = \bar{D}_3^+$ on $\zeta = h$,

$$D_3 = 0 \quad \text{on} \quad \zeta = -h. \tag{12b}$$

The edge boundary conditions of the cylinder are considered as fully simple supports, suitably grounded, and are given as

$$\sigma_1 = u_2 = u_3 = \Phi = 0, \text{ at } x_1 = 0 \text{ and } x_1 = L. \tag{13}$$

There are twenty-two basic equations in the 3D piezoelectricity, as listed in (1)–(8). These are essentially a system of simultaneously partial differential equations with variable coefficients. In the present paper, a meshless collocation method based on the present DRK interpolation is developed for the coupled analysis of functionally graded piezoelectric hollow cylinders under the loading conditions of Cases 1–4 in (9a, b)–(12a, b).

3 Nondimensionalization

In order to scale all the field variables within a close order of magnitude and prevent unexpected numerical instability in the computation process, we define a set of dimensionless coordinates and variables, as follows:

$$\begin{aligned}
&x = x_1/\sqrt{Rh}, \quad \theta = x_2/\sqrt{R/h}, \quad z = \zeta/h, \quad \gamma_\theta = 1 + (hz/R) = x_3/R,\\
&u = u_1/\sqrt{Rh}, \quad v = u_2/\sqrt{Rh}, \quad w = u_3/R,\\
&\sigma_x = \sigma_1/Q, \quad \sigma_\theta = \sigma_2/Q, \quad \tau_{x\theta} = \tau_{12}/Q,\\
&\tau_{xz} = \tau_{13}/(Q\sqrt{h/R}), \quad \tau_{\theta z} = \tau_{23}/(Q\sqrt{h/R}), \quad \sigma_z = \sigma_3 R/(Qh),\\
&D_x = D_1\sqrt{h/R}/e, \qquad D_\theta = D_2\sqrt{h/R}/e, \qquad D_z = D_3/e, \quad \varphi = \Phi e/Qh,
\end{aligned} \tag{14}$$

where R, Q and e stand for the characteristic length, the reference elastic and piezoelectric coefficients, respectively.

In the formulation, the elastic displacements (u, v, w), the transverse shear and normal stresses $(\tau_{xz}, \tau_{\theta z}, \sigma_z)$ and the electric displacement and potential $(D_z,\ \varphi)$ are selected as the primary field variables. The other field variables are the secondary ones, and these can be expressed in terms of the primary variables. Introducing the

set of dimensionless coordinates and variables (14) and using the method of direct elimination, we obtain a set of state space equations in terms of the primary field variables as follows:

$$\frac{\partial}{\partial z}\begin{bmatrix} u \\ v \\ \sigma_z \\ D_z \\ \tau_{xz} \\ \tau_{\theta z} \\ w \\ \varphi \end{bmatrix} = \begin{bmatrix} 0 & 0 & 0 & 0 & k_{15} & 0 & k_{17} & k_{18} \\ 0 & k_{22} & 0 & 0 & 0 & k_{26} & k_{27} & k_{28} \\ k_{31} & k_{32} & k_{33} & k_{34} & k_{17} & k_{27} & k_{37} & 0 \\ 0 & 0 & 0 & k_{44} & k_{18} & k_{28} & 0 & k_{48} \\ k_{51} & k_{52} & k_{53} & k_{54} & k_{44} & 0 & k_{57} & 0 \\ k_{61} & k_{62} & k_{63} & k_{64} & 0 & k_{66} & k_{67} & 0 \\ k_{53} & k_{63} & k_{73} & k_{74} & 0 & 0 & k_{77} & 0 \\ k_{54} & k_{64} & k_{74} & k_{84} & 0 & 0 & k_{87} & 0 \end{bmatrix} \begin{bmatrix} u \\ v \\ \sigma_z \\ D_z \\ \tau_{xz} \\ \tau_{\theta z} \\ w \\ \varphi \end{bmatrix}, \tag{15}$$

where

$$k_{15} = h/\tilde{c}_{55}R, \quad k_{17} = -\partial_x, \quad k_{18} = -\left(h\tilde{e}_{15}/R\tilde{c}_{55}\right)\partial_x,$$

$$k_{22} = h/R\gamma_\theta, \quad k_{26} = h/\tilde{c}_{44}R, \quad k_{27} = -\left(1/\gamma_\theta\right)\partial_\theta, \quad k_{28} = -\left(h\tilde{e}_{24}/R\gamma_\theta\tilde{c}_{44}\right)\partial_\theta,$$

$$k_{31} = \left(\tilde{Q}_{21}/\gamma_\theta\right)\partial_x, \quad k_{32} = \left(\tilde{Q}_{22}/\gamma_\theta^2\right)\partial_\theta, \quad k_{33} = h\left(a_2 - 1\right)/R\gamma_\theta,$$

$$k_{34} = b_2 e/Q\gamma_\theta, \quad k_{37} = \tilde{Q}_{22}/\gamma_\theta^2,$$

$$k_{44} = -h/R\gamma_\theta, \quad k_{48} = (h/R)\left[\left(\tilde{e}_{15}^2/\tilde{c}_{55}\right) + \tilde{\eta}_{11}\right]\partial_{xx} + \left(h/R\gamma_\theta^2\right)\left[\left(\tilde{e}_{24}^2/\tilde{c}_{44}\right) + \tilde{\eta}_{22}\right]\partial_{\theta\theta},$$

$$k_{51} = -\left[\tilde{Q}_{11}\partial_{xx} + \left(\tilde{Q}_{66}/\gamma_\theta^2\right)\partial_{\theta\theta}\right], \quad k_{52} = -\left[\left(\tilde{Q}_{12} + \tilde{Q}_{66}\right)/\gamma_\theta\right]\partial_{x\theta},$$

$$k_{53} = -\left(a_1 h/R\right)\partial_x, \quad k_{54} = -\left(b_1 e/Q\right)\partial_x, \quad k_{57} = -\left(\tilde{Q}_{12}/\gamma_\theta\right)\partial_x,$$

$$k_{61} = -\left[\left(\tilde{Q}_{21} + \tilde{Q}_{66}\right)/\gamma_\theta\right]\partial_{x\theta}, \quad k_{62} = -\left[\tilde{Q}_{66}\partial_{xx} + \left(\tilde{Q}_{22}/\gamma_\theta^2\right)\partial_{\theta\theta}\right],$$

$$k_{63} = -\left(a_2 h/R\gamma_\theta\right)\partial_\theta,$$

$$k_{64} = -\left(b_2 e/Q\gamma_\theta\right)\partial_\theta, \quad k_{66} = -2h/R\gamma_\theta, \quad k_{67} = -\left(\tilde{Q}_{22}/\gamma_\theta^2\right)\partial_\theta,$$

$$k_{73} = Qh^2\bar{\eta}/R^2, \quad k_{74} = \bar{e}eh/R, \quad k_{77} = -a_2 h/R\gamma_\theta,$$

$$k_{84} = -\bar{c}e^2/Q, \quad k_{87} = -b_2 e/Q\gamma_\theta;$$

and the relevant coefficients in the previous terms of l_{ij} and k_{ij} are given in Appendix A.

The in-surface stress and electric displacement components are dependent field variables that can be expressed in terms of the primary variables in the following form

$$\sigma_p = \mathbf{B}_1\mathbf{u} + \mathbf{B}_2 w + \mathbf{B}_3\sigma_z + \mathbf{B}_4 D_z \tag{16}$$

$$\mathbf{d} = \mathbf{B}_5\sigma_s + \mathbf{B}_6\varphi, \tag{17}$$

where

$$\sigma_p = \begin{Bmatrix} \sigma_x \\ \sigma_\theta \\ \tau_{x\theta} \end{Bmatrix}, \quad \mathbf{u} = \begin{Bmatrix} u \\ v \end{Bmatrix}, \quad \sigma_s = \begin{Bmatrix} \tau_{xz} \\ \tau_{\theta z} \end{Bmatrix}, \quad \mathbf{d} = \begin{Bmatrix} D_x \\ D_y \end{Bmatrix},$$

$$\mathbf{B}_1 = \begin{bmatrix} \tilde{Q}_{11}\partial_x & \left(\tilde{Q}_{12}/\gamma_\theta\right)\partial_\theta \\ \tilde{Q}_{21}\partial_x & \left(\tilde{Q}_{22}/\gamma_\theta\right)\partial_\theta \\ \left(\tilde{Q}_{66}/\gamma_\theta\right)\partial_\theta & \tilde{Q}_{66}\partial_x \end{bmatrix},$$

$$\mathbf{B}_2 = \begin{bmatrix} \tilde{Q}_{12}/\gamma_\theta \\ \tilde{Q}_{22}/\gamma_\theta \\ 0 \end{bmatrix}, \quad \mathbf{B}_3 = \begin{bmatrix} a_1 Qh/R \\ a_2 Qh/R \\ 0 \end{bmatrix}, \quad \mathbf{B}_4 = \begin{bmatrix} b_1 e/Q \\ b_2 e/Q \\ 0 \end{bmatrix},$$

$$\mathbf{B}_5 = \begin{bmatrix} (\tilde{e}_{15}h/\tilde{c}_{55}R) & 0 \\ 0 & (\tilde{e}_{24}h/\tilde{c}_{44}R) \end{bmatrix}, \quad \mathbf{B}_6 = \begin{bmatrix} -\left(h/R\right)\left(\tilde{e}_{15}^2/\tilde{c}_{55} + \tilde{\eta}_{11}\right)\partial_x \\ -\left(h/R\gamma_\theta\right)\left(\tilde{e}_{24}^2/\tilde{c}_{44} + \tilde{\eta}_{22}\right)\partial_\theta \end{bmatrix}.$$

The dimensionless form of the boundary conditions on the lateral surfaces are specified as follows:

Case 1. In the cases of closed-circuit and prescribed mechanical load surface conditions,

$$\tau_{xz} = \tau_{\theta z} = \varphi = 0 \quad \text{on} \quad z = \pm 1; \tag{18a}$$

and $\sigma_z = \bar{q}_z^+$ on $z = 1$,

$$\sigma_z = 0 \quad \text{on} \quad z = -1, \tag{18b}$$

where $\bar{q}_z^+ = \bar{q}_3^+ (R/Qh)$.

Case 2. In the cases of closed-circuit and prescribed electric potential surface conditions,

$$\tau_{xz} = \tau_{\theta z} = \sigma_z = 0 \quad \text{on} \quad z = \pm 1; \tag{19a}$$

and $\varphi = \bar{\varphi}^+$ on $z = 1$,

$$\varphi = 0 \quad \text{on} \quad z = -1, \tag{19b}$$

where $\bar{\varphi}^+ = \bar{\Phi}^+ (e/Qh)$.

Case 3. In the cases of open-circuit and prescribed mechanical load surface conditions,

$$\tau_{xz} = \tau_{\theta z} = D_z = 0 \quad \text{on} \quad z = \pm 1; \tag{20a}$$

and $\sigma_z = \bar{q}_z^+$ on $z = 1$,

$$\sigma_z = 0 \quad \text{on} \quad z = -1. \tag{20b}$$

Case 4. In the cases of open-circuit and prescribed electric displacement surface conditions,

$$\tau_{xz} = \tau_{\theta z} = \sigma_z = 0 \quad \text{on} \quad z = \pm 1; \tag{21a}$$

and $D_z = \bar{D}_z^+$ on $z = 1$,

$$D_z = 0 \quad \text{on} \quad z = -1, \tag{21b}$$

where $\bar{D}_z^+ = \bar{D}_3^+ / e$.

At the edges, the following quantities are satisfied:

$$\sigma_x = v = w = \varphi = 0, \text{ at } x = 0 \text{ and } x = L/\sqrt{Rh}. \tag{22}$$

4 The DRK Interpolation

In the present paper, a meshless DRK interpolation-based collocation method is developed for the analysis of FG piezoelectric hollow cylinders under the electro-mechanical loads (Cases 1–4). The present DRK interpolation functions and their relevant derivatives are described, as follows.

4.1 Reproducing kernel interpolation functions

It is assumed that there are *NP* discrete points randomly selected and located at $z = z_1, z_2, \cdots, z_{NP}$, respectively, in the domain Ω. In the present formulation, a function $F(z)$ is interpolated as $F^a(z)$ and defined as

$$\begin{aligned} F^a(z) &= \sum_{l=1}^{NP} N_l(z) F_l \\ &= \sum_{l=1}^{NP} \left[\bar{\phi}_l(z) + \hat{\phi}_l(z)\right] F_l, \end{aligned} \tag{23}$$

where $N_l(z)$ is the shape function of $F^a(z)$ corresponding to the related node at $z = z_l$; F_l is the nodal value of $F^a(z)$ at $z = z_l$; $\hat{\phi}_l(z)$ (l=1, 2,…, *NP*) denote the primitive functions used to introduce Kronecker delta properties; $\bar{\phi}_l(z)$ (l=1, 2,…, *NP*) denote the enrichment functions for imposing the n^{th}-order reproducing conditions, and are given by $\bar{\phi}_l(z) = w_a(z-z_l)\mathbf{P}^T(z-z_l)\bar{\mathbf{b}}(z)$; $\mathbf{P}^T(z-z_l)$ denotes the polynomial basis, and is given as $\mathbf{P}^T(z-z_l) = \begin{bmatrix}1 & (z-z_l) & (z-z_l)^2 & \cdots & (z-z_l)^n\end{bmatrix}$; n denotes the highest order of the basis functions; $\bar{\mathbf{b}}(z)$ is the undetermined function vector, and will be determined by satisfying the reproducing conditions; and $w_a(z-z_l)$ is the weight function centered at z_l, with a support size a.

By selecting the complete n^{th}-order polynomials as the basis functions to be reproduced, we obtain a set of reproducing conditions to determine the undetermined functions of $\bar{b}_i(z)$ ($i = 1, 2, \cdots, n+1$) in (23). The reproducing conditions are give as

$$\sum_{l=1}^{NP} \left[\bar{\phi}_l(z) + \hat{\phi}_l(z)\right] z_l^r = z^r \quad r \le n. \tag{24}$$

Equation (24) represents (n+1) reproducing conditions, and can be rearranged in the explicit form of

$$r = 0: \sum_{l=1}^{NP} \bar{\phi}_l(z) = 1 - \sum_{l=1}^{NP} \hat{\phi}_l(z), \tag{25}$$

$$r=1:\ \sum_{l=1}^{NP}\bar{\phi}_l(z)(z-z_l)=z\sum_{l=1}^{NP}\bar{\phi}_l(z)-\sum_{l=1}^{NP}\bar{\phi}_l(z)z_l=0-\sum_{l=1}^{NP}\hat{\phi}_l(z)(z-z_l) \tag{26}$$

$$r=2:\ \sum_{l=1}^{NP}\bar{\phi}_l(z)(z-z_l)^2=z^2\sum_{l=1}^{NP}\bar{\phi}_l(z)-2z\sum_{l=1}^{NP}\bar{\phi}_l(z)z_l+\sum_{l=1}^{NP}\bar{\phi}_l(z)z_l^2 = 0-\sum_{l=1}^{NP}\hat{\phi}_l(z)(z-z_l)^2 \tag{27}$$

$$\vdots$$

$$r=n:\ \sum_{l=1}^{NP}\bar{\phi}_l(z)(z-z_l)^n=0-\sum_{l=1}^{NP}\hat{\phi}_l(z)(z-z_l)^n. \tag{28}$$

The matrix form of the previous reproducing conditions is given as

$$\begin{aligned}\sum_{l=1}^{NP}\mathbf{P}(z-z_l)\bar{\phi}_l(z)&=\sum_{l=1}^{NP}\mathbf{P}(z-z_l)w_a(z-z_l)\mathbf{P}^T(z-z_l)\bar{\mathbf{b}}(z)\\&=\mathbf{P}(\mathbf{0})-\sum_{l=1}^{NP}\mathbf{P}(z-z_l)\hat{\phi}_l(z),\end{aligned} \tag{29}$$

where $\mathbf{P}(\mathbf{0})=\begin{bmatrix}1 & 0 & 0 & \cdots & 0\end{bmatrix}^T$.

According to the reproducing conditions in (29), we may obtain the undetermined function vector $\bar{\mathbf{b}}(z)$ in the following form

$$\bar{\mathbf{b}}(z)=\mathbf{A}^{-1}(z)\left[\mathbf{P}(\mathbf{0})-\sum_{l=1}^{NP}\mathbf{P}(z-z_l)\hat{\phi}_l(z)\right], \tag{30}$$

where $\mathbf{A}(z)=\sum_{l=1}^{NP}\mathbf{P}(z-z_l)w_a(z-z_l)\mathbf{P}^T(z-z_l)$.

Substituting (30) into (23) yields the shape functions of $F^a(z)$ in the form of

$$N_l(z)=\bar{\phi}_l(z)+\hat{\phi}_l(z)\quad(l=1,2,\ldots,NP), \tag{31}$$

where $\bar{\phi}_l(z)=w_a(z-z_l)\mathbf{P}^T(z-z_l)\mathbf{A}^{-1}(z)\left[\mathbf{P}(\mathbf{0})-\sum_{l=1}^{NP}\mathbf{P}(z-z_l)\hat{\phi}(z)\right]$.

It is noted that if we select a set of primitive functions satisfying the Kronecker delta properties (i.e., $\hat{\phi}_l(z_k)=\delta_{lk}$), then according to (31) the enrichment functions should vanish at all the nodes (i.e., $\bar{\phi}_l(z_k)=0$). A set of the shape functions, $N_l(z)$,

with Kronecker delta properties is thus obtained (i.e., $N_l(z_k) = \delta_{lk}$). It is apparent that there are many possibilities to select the set of primitive functions. A set of finite element shape functions has been suggested by Huerta, Fermandez and Mendez (2000), while a set of normalized weight functions for which the support size of each sampling node does not cover any neighbouring nodes has been suggested by Chen et al. (2003). In the present paper, a function of the quartic spline with its support size not covering any neighbouring nodes is assigned to be the primitive function for each sampling node.

It is realized from (31) that $N_l(z)$ vanishes when z is not in the support of the node at $z = z_l$. The influence of the shape functions in the support of each sampling node monotonically decreases as the relative distance to the node increases, and this preserves the local character of the present scheme.

4.2 Derivatives of reproducing kernel interpolation functions

Since the reproducing kernel interpolation function in the present scheme, $F^a(z)$, is given in (23), the first-order derivative of $F^a(z)$ with respect to z is then expressed as

$$\begin{aligned} \frac{dF^a(z)}{dz} &= \sum_{l=1}^{NP} N_l^{(1)}(z) F_l \\ &= \sum_{l=1}^{NP} \left(\bar{\phi}_l^{(1)}(z) + \frac{d\hat{\phi}_l(z)}{dz} \right) F_l, \end{aligned} \tag{32}$$

where $N_l^{(1)}(z)$ (l=1,2,..., NP) denote the shape functions of the first-order derivative of $F^a(z)$ with respect to z; and $\bar{\phi}_l^{(1)}(z) = w_a(z-z_l)\mathbf{P}^T(z-z_l)\bar{\mathbf{b}}_1(z)$.

The differential reproducing conditions for a set of complete n^{th}-order polynomials are given as

$$\sum_{l=1}^{NP} \left[\bar{\phi}_l^{(1)}(z) + \frac{d\hat{\phi}_l(z)}{dz} \right] z_l^r = r z^{r-1} \quad r \le n. \tag{33}$$

Equation (33) represents (n+1) differential reproducing conditions, and can be rearranged in the explicit form of

$$r = 0: \sum_{l=1}^{NP} \bar{\phi}_l^{(1)}(z) = 0 - \sum_{l=1}^{NP} \frac{d\hat{\phi}_l(z)}{dz}, \tag{34}$$

$$r=1:\ \sum_{l=1}^{NP}\bar{\phi}_l^{(1)}(z)(z-z_l)=z\sum_{l=1}^{NP}\bar{\phi}_l^{(1)}(z)-\sum_{l=1}^{NP}\bar{\phi}_l^{(1)}(z)z_l$$
$$=-1-\sum_{l=1}^{NP}\frac{d\hat{\phi}_l(z)}{dz}(z-z_l) \quad (35)$$

$$r=2:\ \sum_{l=1}^{NP}\bar{\phi}_l^{(1)}(z)(z-z_l)^2=z^2\sum_{l=1}^{NP}\bar{\phi}_l^{(1)}(z)-2z\sum_{l=1}^{NP}\bar{\phi}_l^{(1)}(z)z_l+\sum_{l=1}^{NP}\bar{\phi}_l^{(1)}(z)z_l^2$$
$$=0-\sum_{l=1}^{NP}\frac{d\hat{\phi}_l(z)}{dz}(z-z_l)^2 \quad (36)$$

$$\vdots$$

$$r=n:\ \sum_{l=1}^{NP}\bar{\phi}_l^{(1)}(z)(z-z_l)^n=0-\sum_{l=1}^{NP}\frac{d\hat{\phi}_l(z)}{dz}(z-z_l)^n. \quad (37)$$

Equations (34)–(37) are rewritten in the matrix form of

$$\sum_{l=1}^{NP}\mathbf{P}(z-z_l)\bar{\phi}_l^{(1)}(z)=\sum_{l=1}^{NP}\mathbf{P}(z-z_l)w_a(z-z_l)\mathbf{P}^T(z-z_l)\bar{\mathbf{b}}_1(z)$$
$$=-\mathbf{P}^{(1)}(\mathbf{0})-\sum_{l=1}^{NP}\mathbf{P}(z-z_l)\frac{d\hat{\phi}_l(z)}{dz}, \quad (38)$$

where $(-1)\left[\mathbf{P}^{(1)}(\mathbf{0})\right]=-\left.\frac{d\mathbf{P}(z-z_l)}{dz}\right|_{z=z_l}=\begin{bmatrix}0 & -1 & 0 & \cdots & 0\end{bmatrix}^T$.

The undetermined function vector $\bar{\mathbf{b}}_1(z)$ can then be obtained and given by

$$\bar{\mathbf{b}}_1(z)=\mathbf{A}^{-1}(z)\left[-\mathbf{P}^{(1)}(\mathbf{0})-\sum_{l=1}^{NP}\mathbf{P}(z-z_l)\frac{d\hat{\phi}_l(z)}{dz}\right]. \quad (39)$$

Substituting (39) into (32) yields the shape functions of the first-order derivative of the RK interpolation functions with respect to x in the form of

$$N_l^{(1)}(z)=\bar{\phi}_l^{(1)}(z)+\frac{d\hat{\phi}_l(z)}{dz}, \quad (40)$$

where $\bar{\phi}_l^{(1)}(z)=w_a(z-z_l)\mathbf{P}^T(z-z_l)\mathbf{A}^{-1}(z)\left[-\mathbf{P}^{(1)}(\mathbf{0})-\sum_{l=1}^{NP}\mathbf{P}(z-z_l)\frac{d\hat{\phi}_l(z)}{dz}\right]$.

Carrying out the same derivation for the higher-order derivatives of $F^a(z)$ leads to

$$\frac{d^k F^a(z)}{dz^k} = \sum_{l=1}^{NP} N_l^{(k)}(z) F_l, \tag{41}$$

where $N_l^{(k)}(z) = \bar{\phi}_l^{(k)}(z) + \frac{d^k \hat{\phi}_l(z)}{dz^k}$,

$$\bar{\phi}_l^{(k)}(z) = w_a(z-z_l)\,\mathbf{P}^T(z-z_l)\,\mathbf{A}^{-1}(z)\left[(-1)^k \mathbf{P}^{(k)}(\mathbf{0}) - \sum_{l=1}^{NP} \mathbf{P}(z-z_l)\,\frac{d^k \hat{\phi}_l(z)}{dz^k}\right],$$

$$\mathbf{P}^{(k)}(\mathbf{0}) = \left.\frac{d^k \mathbf{P}(z-z_l)}{dz^k}\right|_{z=z_l}.$$

4.3 Weight functions

In implementing the present scheme, the weight function and the primitive function at each sampling node must be selected in advance. The normalized Gaussian function and the quartic spline function are adopted as the weight function and the primitive function, respectively, and are given as

Normalized Gaussian function:

$$w(s) = \begin{cases} \frac{e^{-(s/\alpha)^2} - e^{-(1/\alpha)^2}}{1 - e^{-(1/\alpha)^2}} & \text{for} \quad s \le 1 \\ 0 & \text{for} \quad s > 1 \end{cases}, \tag{42}$$

Quartic spline:

$$w(s) = \begin{cases} -3s^4 + 8s^3 - 6s^2 + 1 & \text{for} \quad s \le 1 \\ 0 & \text{for} \quad s > 1 \end{cases}, \tag{43}$$

where $w_a(z-z_l) = w(s)$ and $s = |z-z_l|/a$. In the literature α is usually set as 0.3. It is noted that a very small value of a may result in an unexpected numerical error when the calculation for the coefficients of the system matrix is performed. On the other hand, the value of a also has to be small enough to preserve the local character of the present scheme. Hence, a compromise range of the value of a will be studied later to ensure the accuracy and convergence of the present scheme.

5 Applications

The static behavior of the simply-supported, FG piezoelectric hollow cylinders with open-circuit and closed-circuit surface conditions and operating under electro-mechanical loads (Cases 1–4) is studied. The applied electro-mechanical loads are expanded as the double Fourier series in the form of

$$\bar{q}_3^+ = \sum_{\hat{m}=1}^{\infty}\sum_{\hat{n}=1}^{\infty}\left(\bar{q}_3^+\right)_{\hat{m}\hat{n}}\sin\left(\hat{m}\pi x_1/L\right)\cos\left(\hat{n}x_2\right) \text{ or}$$

$$\bar{q}_z^+ = \sum_{\hat{m}=1}^{\infty}\sum_{\hat{n}=1}^{\infty}\left(\bar{q}_z^+\right)_{\hat{m}\hat{n}}\sin\left(\tilde{m}x\right)\cos\left(\tilde{n}\theta\right) \quad (44a)$$

$$\bar{\Phi}^+ = \sum_{\hat{m}=1}^{\infty}\sum_{\hat{n}=1}^{\infty}\left(\bar{\Phi}^+\right)_{\hat{m}\hat{n}}\sin\left(\hat{m}\pi x_1/L\right)\cos\left(\hat{n}x_2\right) \text{ or}$$

$$\bar{\varphi}^+ = \sum_{\hat{m}=1}^{\infty}\sum_{\hat{n}=1}^{\infty}\left(\bar{\varphi}^+\right)_{\hat{m}\hat{n}}\sin\left(\tilde{m}x\right)\cos\left(\tilde{n}\theta\right), \quad (44b)$$

$$\bar{D}_3^+ = \sum_{\hat{m}=1}^{\infty}\sum_{\hat{n}=1}^{\infty}\left(\bar{D}_3^+\right)_{\hat{m}\hat{n}}\sin\left(\hat{m}\pi x_1/L\right)\cos\left(\hat{n}x_2\right) \text{ or}$$

$$\bar{D}_z^+ = \sum_{\hat{m}=1}^{\infty}\sum_{\hat{n}=1}^{\infty}\left(\bar{D}_z^+\right)_{\hat{m}\hat{n}}\sin\left(\tilde{m}x\right)\cos\left(\tilde{n}\theta\right), \quad (44c)$$

where $\tilde{m} = \hat{m}\pi\sqrt{Rh}/L$, $\tilde{n} = \hat{n}\sqrt{h/R}$ in which $\hat{m}$ and $\hat{n}$ are positive integers.

5.1 The method of double Fourier series expansion

The method of double Fourier series expansion is applied to reduce the system of partial differential equations (15) to a system of ordinary differential equations. By satisfying the edge boundary conditions, we express the primary variables in the following form

$$(u, \tau_{xz}) = \sum_{\hat{m}=1}^{\infty}\sum_{\hat{n}=1}^{\infty}\left(u_{\hat{m}\hat{n}}(z), \tau_{xz\hat{m}\hat{n}}(z)\right)\cos\tilde{m}x\cos\tilde{n}\theta, \quad (45)$$

$$(v, \tau_{\theta z}) = \sum_{\hat{m}=1}^{\infty}\sum_{\hat{n}=1}^{\infty}\left(v_{\hat{m}\hat{n}}(z), \tau_{\theta z\hat{m}\hat{n}}(z)\right)\sin\tilde{m}x\sin\tilde{n}\theta, \quad (46)$$

$$(w, \sigma_z, \varphi, D_z) = \sum_{\hat{m}=1}^{\infty}\sum_{\hat{n}=1}^{\infty}\left(w_{\hat{m}\hat{n}}(z), \sigma_{z\hat{m}\hat{n}}(z), \varphi_{\hat{m}\hat{n}}(z), D_{z\hat{m}\hat{n}}(z)\right)\sin\tilde{m}x\cos\tilde{n}\theta. \quad (47)$$

For brevity, the symbols of summation are omitted in the following derivation. Using the set of dimensionless coordinates and field variables (14) and substituting (45)–(47) in (15), we have the resulting equations, as follows:

$$\frac{d}{dz}\begin{bmatrix} u_{\hat{m}\hat{n}} \\ v_{\hat{m}\hat{n}} \\ \sigma_{z\hat{m}\hat{n}} \\ D_{z\hat{m}\hat{n}} \\ \tau_{xz\hat{m}\hat{n}} \\ \tau_{\theta z\hat{m}\hat{n}} \\ w_{\hat{m}\hat{n}} \\ \varphi_{\hat{m}\hat{n}} \end{bmatrix} = \begin{bmatrix} 0 & 0 & 0 & 0 & \bar{k}_{15} & 0 & \bar{k}_{17} & \bar{k}_{18} \\ 0 & \bar{k}_{22} & 0 & 0 & 0 & \bar{k}_{26} & \bar{k}_{27} & \bar{k}_{28} \\ \bar{k}_{31} & \bar{k}_{32} & \bar{k}_{33} & \bar{k}_{34} & -\bar{k}_{17} & -\bar{k}_{27} & \bar{k}_{37} & 0 \\ 0 & 0 & 0 & \bar{k}_{44} & -\bar{k}_{18} & -\bar{k}_{28} & 0 & \bar{k}_{48} \\ \bar{k}_{51} & \bar{k}_{52} & \bar{k}_{53} & \bar{k}_{54} & \bar{k}_{44} & 0 & \bar{k}_{57} & 0 \\ \bar{k}_{61} & \bar{k}_{62} & \bar{k}_{63} & \bar{k}_{64} & 0 & \bar{k}_{66} & \bar{k}_{67} & 0 \\ -\bar{k}_{53} & -\bar{k}_{63} & \bar{k}_{73} & \bar{k}_{74} & 0 & 0 & \bar{k}_{77} & 0 \\ -\bar{k}_{54} & -\bar{k}_{64} & \bar{k}_{74} & \bar{k}_{84} & 0 & 0 & \bar{k}_{87} & 0 \end{bmatrix} \begin{bmatrix} u_{\hat{m}\hat{n}} \\ v_{\hat{m}\hat{n}} \\ \sigma_{z\hat{m}\hat{n}} \\ D_{z\hat{m}\hat{n}} \\ \tau_{xz\hat{m}\hat{n}} \\ \tau_{\theta z\hat{m}\hat{n}} \\ w_{\hat{m}\hat{n}} \\ \varphi_{\hat{m}\hat{n}} \end{bmatrix}, \quad (48)$$

where $\bar{l}_{ij}$ and $\bar{k}_{ij}$ are given in Appendix B.

Equation (48) represents a system of eight simultaneously linear ordinary differential equations in terms of eight primary variables. A meshfree collocation method based on the present DRK interpolation is applied to determine the primary variables in the elastic and electric fields. Once these primary variables are determined, the dependent variables can then be calculated using (16)–(17).

5.2 Multilayered hollow cylinders

The present DRK interpolation-based collocation method is applied to the coupled electro-elastic analysis of multilayered hybrid elastic and piezoelectric cylinders. Selecting N_p nodal points along the thickness coordinate from bottom to top surfaces of the m^{th}-layer and applying the present DRK interpolation functions to (48) at each nodal point, we obtain

$$\left(\sum_{l=1}^{N_p} N_l^{(1)}(z_p^{(m)})\left(\hat{F}_i^{(m)}\right)_l\right) - \bar{k}_{ij}^{(m)}\left(\sum_{l=1}^{N_p} N_l(z_p^{(m)})\left(\hat{F}_j^{(m)}\right)_l\right) = 0$$
$$\text{for } i,j = 1,2,3,\cdots,8 \text{ and } p = 1,2,3,\cdots,N_p, \quad (49)$$

where $\hat{\mathbf{F}}^{(m)} = \left\{\hat{u}^{(m)} \quad \hat{v}^{(m)} \quad \hat{\sigma}_z^{(m)} \quad \hat{D}_z^{(m)} \quad \hat{\tau}_{xz}^{(m)} \quad \hat{\tau}_{\theta z}^{(m)} \quad \hat{w}^{(m)} \quad \hat{\varphi}^{(m)}\right\}^T$ and $\left(\hat{F}_j^{(m)}\right)_l$ denotes the nodal value of j^{th} primary variable in $\hat{\mathbf{F}}^{(m)}$ at the l^{th} nodal point of the m^{th}-layer. In the present analysis, we let $\Delta x_3^{(m)} = 2h^{(m)}/(N_p-1)$, $m = 1,2,3\cdots,NL$ where $2h^{(m)}$ denotes the thickness of the m^{th}-layer and $2h^{(m)} = \zeta_{N_p}^{(m)} - \zeta_1^{(m)}$.

The DRK interpolation functions are applied to the boundary conditions on the lateral surfaces as follows:

Case 1. $\left(\hat{F}_5^{(1)}\right)_1 = 0$, $\left(\hat{F}_6^{(1)}\right)_1$=0, $\left(\hat{F}_3^{(1)}\right)_1$=0, $\left(\hat{F}_8^{(1)}\right)_1$=0,

$$\left(\hat{F}_5^{(NL)}\right)_{N_p} = 0, \quad \left(\hat{F}_6^{(NL)}\right)_{N_p} = 0, \quad \left(\hat{F}_3^{(NL)}\right)_{N_p} = \bar{q}_0, \quad \left(\hat{F}_8^{(NL)}\right)_{N_p} = 0,$$

where

$$\bar{q}_0 = \left(\bar{q}_3^+\right)_{\hat{m}\hat{n}} R/Qh. \tag{50a}$$

Case 2. $\left(\hat{F}_5^{(1)}\right)_1 = 0$, $\left(\hat{F}_6^{(1)}\right)_1$=0, $\left(\hat{F}_3^{(1)}\right)_1$=0, $\left(\hat{F}_8^{(1)}\right)_1$=0,

$$\left(\hat{F}_5^{(NL)}\right)_{N_p} = 0, \quad \left(\hat{F}_6^{(NL)}\right)_{N_p} = 0, \quad \left(\hat{F}_3^{(NL)}\right)_{N_p} = 0, \quad \left(\hat{F}_8^{(NL)}\right)_{N_p} = \bar{\varphi}_0,$$

where

$$\bar{\varphi}_0 = \left(\bar{\Phi}^+\right)_{\hat{m}\hat{n}} e/Qh. \tag{50b}$$

Case 3. $\left(\hat{F}_5^{(1)}\right)_1 = 0$, $\left(\hat{F}_6^{(1)}\right)_1$=0, $\left(\hat{F}_3^{(1)}\right)_1$=0, $\left(\hat{F}_4^{(1)}\right)_1$=0,

$$\left(\hat{F}_5^{(NL)}\right)_{N_p} = 0, \quad \left(\hat{F}_6^{(NL)}\right)_{N_p} = 0, \quad \left(\hat{F}_3^{(NL)}\right)_{N_p} = \bar{q}_0, \quad \left(\hat{F}_4^{(NL)}\right)_{N_p} = 0, \tag{50c}$$

Case 4. $\left(\hat{F}_5^{(1)}\right)_1 = 0$, $\left(\hat{F}_6^{(1)}\right)_1$=0, $\left(\hat{F}_3^{(1)}\right)_1$=0, $\left(\hat{F}_4^{(1)}\right)_1$=0,

$$\left(\hat{F}_5^{(NL)}\right)_{N_p} = 0, \quad \left(\hat{F}_6^{(NL)}\right)_{N_p} = 0, \quad \left(\hat{F}_3^{(NL)}\right)_{N_p} = 0, \quad \left(\hat{F}_4^{(NL)}\right)_{N_p} = \bar{D}_0,$$

where

$$\bar{D}_0 = \left(\bar{D}_3^+\right)_{\hat{m}\hat{n}} / e. \tag{50d}$$

The continuity conditions at interfaces between adjacent layers are also given by

$$\left(\hat{F}_i^{(m)}\right)_{N_p} = \left(\hat{F}_i^{(m+1)}\right)_1 \text{ for } i = 1,2,3,\cdots,8 \text{ and } m = 1,2,\cdots,(NL-1). \tag{51}$$

By means of an assembly process similar to that used in the FEM, we may combine (49)–(51) to construct a set of system equations of the multilayered hollow cylinder which consists of $[8\text{x}NL\text{x}(N_p-1)]$ simultaneously algebraic equations in terms of $[8\text{x}NL\text{x}(N_p-1)]$ unknowns. The primary variables at each nodal point can then be obtained by solving the previously obtained equations. As a consequence, the secondary variables can be calculated using (16) and (17), and the through-thickness distributions of various variables can be interpolated using (23).

5.3 Functionally graded hollow cylinders

In the present paper, the material properties of the FG piezoelectric hollow cylinder are assumed to obey an exponent-law dependent on the thickness coordinate of the cylinder, and are given as

$$m_{ij}(z) = m_{ij}^{(b)} e^{\kappa[(z+1)/2]}, \tag{52}$$

where the superscript b in parentheses denotes the bottom surface of the cylinder; and κ denotes the material-property gradient index, which represents the degree of the material-property gradient along the thickness coordinate. It is noted that $\kappa = 0$ corresponds to the homogeneous material, $\kappa < 0$ to the graded soft material, and $\kappa > 0$ to the graded stiff material.

Selecting NP nodal points along the thickness coordinate from bottom to top surfaces of the hollow cylinder and applying the present DRK interpolation to (48) at each nodal point, we obtain

$$\left(\sum_{l=1}^{NP} N_l^{(1)}(z_r)\left(\hat{F}_i\right)_l\right) - \bar{k}_{ij}\left(\sum_{l=1}^{NP} N_l(z_r)\left(\hat{F}_j\right)_l\right) = 0$$
$$\text{for } i,j = 1,2,3,\cdots,8 \text{ and } r = 1,2,3,\cdots,NP \tag{53}$$

Similarly, the DRK interpolation functions are applied to the boundary conditions on the lateral surfaces of the cylinder, as follows: Case 1. $\left(\hat{F}_5\right)_1 = 0$, $\left(\hat{F}_6\right)_1$=0, $\left(\hat{F}_3\right)_1$=0, $\left(\hat{F}_8\right)_1$=0,

$$\left(\hat{F}_5\right)_{NP} = 0, \quad \left(\hat{F}_6\right)_{NP} = 0, \quad \left(\hat{F}_3\right)_{NP} = \bar{q}_0, \quad \left(\hat{F}_8\right)_{NP} = 0. \tag{54a}$$

Case 2. $\left(\hat{F}_5\right)_1 = 0$, $\left(\hat{F}_6\right)_1$=0, $\left(\hat{F}_3\right)_1$=0, $\left(\hat{F}_8\right)_1$=0,

$$\left(\hat{F}_5\right)_{NP} = 0, \quad \left(\hat{F}_6\right)_{NP} = 0, \quad \left(\hat{F}_3\right)_{NP} = 0, \quad \left(\hat{F}_8\right)_{NP} = \bar{\varphi}_0. \tag{54b}$$

Case 3. $\left(\hat{F}_5\right)_1 = 0$, $\left(\hat{F}_6\right)_1$=0, $\left(\hat{F}_3\right)_1$=0, $\left(\hat{F}_4\right)_1$=0,

$$\left(\hat{F}_5\right)_{NP} = 0, \quad \left(\hat{F}_6\right)_{NP} = 0, \quad \left(\hat{F}_3\right)_{NP} = \bar{q}_0, \quad \left(\hat{F}_4\right)_{NP} = 0. \tag{54c}$$

Case 4. $\left(\hat{F}_5\right)_1 = 0$, $\left(\hat{F}_6\right)_1$=0, $\left(\hat{F}_3\right)_1$=0, $\left(\hat{F}_4\right)_1$=0,

$$\left(\hat{F}_5\right)_{NP} = 0, \quad \left(\hat{F}_6\right)_{NP} = 0, \quad \left(\hat{F}_3\right)_1 = 0, \quad \left(\hat{F}_4\right)_{NP} = \bar{D}_0. \tag{54d}$$

Again, by means of an assembly process similar to that used in the FEM, we may combine (53) and (54) to construct a set of system equations of the FG hollow cylinder which consists of $[8\text{x}(NP-1)]$ simultaneously algebraic equations in terms of

$[8\mathrm{x}(NP-1)]$ unknowns. The primary variables at each nodal point can then be obtained by solving the previously obtained equations. As a consequence, the secondary variables can be calculated using (16) and (17) and the through-thickness distributions of various variables can be interpolated using (23).

Table 1: Elastic, piezoelectric and dielectric properties of composite and piezoelectric materials

Moduli	PVDT	Graphite/Epoxy	PZT-4
c_{11}(Gpa)	3.0	183.433	138.499
c_{22}	3.0	11.662	138.499
c_{33}	3.0	11.662	114.745
c_{12}	1.5	4.363	77.371
c_{13}	1.5	4.363	73.643
c_{23}	1.5	3.918	73.643
c_{44}	0.75	2.870	25.6
c_{55}	0.75	7.170	25.6
c_{66}	0.75	7.170	30.6
$e_{24}\left(C/m^2\right)$	0.0	0.000	12.72
e_{15}	0.0	0.000	12.72
e_{31}	-0.15e-02	0.000	-5.2
e_{32}	0.285e-01	0.000	-5.2
e_{33}	-0.51e-01	0.000	15.08
$\eta_{11}\left(F/m\right)$	0.1062e-09	1.53e-08	1.306e-08
η_{22}	0.1062e-09	1.53e-08	1.306e-08
η_{33}	0.1062e-09	1.53e-08	1.151e-08

6 Illustrative examples

6.1 Single-layer homogeneous piezoelectric hollow cylinders

For comparison purposes, the present DRK interpolation-based collocation method is applied to the coupled analysis of simply-supported, single-layer homogeneous piezoelectric hollow cylinders with closed-circuit boundary conditions and under axisymmetric electro-mechanical loads. The mechanical load ($\bar{q}_3^+ = q_0 \sin\left(\pi x_1/L\right), q_0 = -1\mathrm{N/m}^2$) and electric potential ($\Phi^+ = \varphi_0 \sin\left(\pi x_1/L\right), \varphi_0 = 1\mathrm{V}$) are applied on the outer surface of the cylinder, respectively (i.e., Cases 1 and 2 with $\hat{m} = 1$, $\hat{n}$=0). The cylinder is considered to be composed of polyvinyledene fluoride (PVDF) polarized along the radial direction. The geometric parameter of $R/2h$ is taken as $R/2h$ =4. The elastic, piezoelectric and dielectric properties of the PVDF material

are given in Table 1. A set of normalized variables is defined as the same form of that used in earlier research (kapuria, Sengupta and Dumir, 1997a; Wu, Syu and Lo, 2007), and is given as follows:

In the cases of applied mechanical loads,

$$(\bar{u},\bar{w}) = (u_1/2h, u_3/2h) \,/\, \left(|q_0| S^2/E_T\right),$$

$$(\bar{D}_x,\bar{D}_z) = (10D_1 S/\,|q_0|\,|d_T|\,, D_3/\,|q_0|\,S\,|d_T|),$$

$$(\bar{\sigma}_x,\bar{\sigma}_\theta,\bar{\sigma}_z,\bar{\tau}_{xz}) = (\sigma_1,\sigma_2/S,\sigma_3,\tau_{13}S)\,/\,|q_0|\,,$$

$$\bar{\varphi} = 1000\Phi E_T\,|d_T|\,/2h\,|q_0|\,. \tag{55}$$

In the cases of applied electrical potential,

$$(\bar{u},\bar{w}) = (u_1/\varphi_0 S\,|d_T|\,, u_3/\varphi_0 S\,|d_T|)\,,$$

$$(\bar{D}_x,\bar{D}_z) = \left(2hD_1 S/100\varphi_0 E_T\,|d_T|^2\,, 2hD_3/\varphi_0 E_T\,|d_T|^2\right),$$

$$(\bar{\sigma}_x,\quad \bar{\sigma}_\theta) = (2hS\sigma_1/\varphi_0 E_T\,|d_T|\,,\quad 2hS\sigma_2/\varphi_0 E_T\,|d_T|)\,,$$

$$(\bar{\sigma}_z,\quad \bar{\tau}_{xz}) = \left(2hS^2\sigma_3/\varphi_0 E_T\,|d_T|\,,\quad 20hS^2\tau_{13}/\varphi_0 E_T\,|d_T|\right),$$

$$\bar{\varphi} = \Phi/\varphi_0, \tag{56}$$

and $S = R/2h$, $E_T = 2.0$GPa, $|d_T| = 30\text{x}10^{-12}$C / N.

Tables 2–3 show the elastic and electric field variables induced at crucial positions of the single-layer piezoelectric cylinder under the mechanical load and electric potential, respectively. In the implementation, a uniform spacing (Δz) for each pair of neighboring nodal points is used, where $\Delta z = 2$ / (NP - 1) and $\Delta z = \Delta x_3/h$. The effects of the highest order of basis functions (n) and the support size (a) on the present solutions are presented, where the values of (n, a) are taken to be (2, 2.1Δz), (3, 3.1Δz) and (4, 4.1Δz). The total number of nodal points is taken as NP=7, 9, 11, 21. The accuracy and rate of convergence of the present method are validated by comparing the present solutions with the available 3D solutions obtained by Kapuria, Sengupta and Dumir (1997a) using the modified Frobenius series method and the 3D asymptotic solutions by Wu, Syu and Lo (2007) using the perturbation method. It is shown from Tables 2–3 that the present solutions with (n=3, a=3.1Δz) and (n=4, a=4.1Δz) are in excellent agreement with the available 3D solutions.

Table 2: The elastic and electric field variables at crucial positions of single-layer piezoelectric hollow cylinders under mechanical load (Case 1 with $\hat{m}=1$, $\hat{n}=0$ and $R/2h$=4)

n	a	Theories	-$\bar{u}\left(0,-h\right)$	-$\bar{w}\left(\frac{L}{2},-h\right)$	-$\bar{D}_z\left(\frac{L}{2},-h\right)$	-$\bar{\sigma}_x\left(\frac{L}{2},-h\right)$	-$\bar{\sigma}_\theta\left(\frac{L}{2},-h\right)$	-$\bar{\tau}_{xz}\left(0,0\right)$	-$\bar{\sigma}_z\left(\frac{L}{2},0\right)$	-$\bar{\varphi}\left(\frac{L}{2},0\right)$
2	2.1Δz	Present *NP*= 7	0.646800	1.107194	0.820820	-0.384845	1.234774	0.071501	0.585915	1.622457
		NP= 9	0.646334	1.106352	0.820561	-0.384655	1.233822	0.070927	0.585662	1.545054
		NP=11	0.646075	1.105897	0.820378	-0.384524	1.233309	0.071313	0.585845	1.592037
		NP=21	0.645675	1.105206	0.820077	-0.384301	1.232535	0.071222	0.585840	1.578582
3	3.1Δz	Present *NP*= 7	0.645506	1.104919	0.819944	-0.384201	1.232213	0.071262	0.585902	1.582129
		NP= 9	0.645516	1.104935	0.819954	-0.384208	1.232232	0.071239	0.585857	1.580362
		NP=11	0.645519	1.104940	0.819957	-0.384210	1.232237	0.071250	0.585874	1.581213
		NP=21	0.645521	1.104943	0.819959	-0.384211	1.232241	0.071247	0.585869	1.580984
4	4.1Δz	Present *NP*= 7	0.645501	1.104909	0.819941	-0.384200	1.232203	0.071250	0.585873	1.581207
		NP= 9	0.645513	1.104930	0.819952	-0.384207	1.232226	0.071246	0.585870	1.580946
		NP=11	0.645517	1.104937	0.819956	-0.384210	1.232234	0.071248	0.585870	1.581036
		NP=21	0.645521	1.104943	0.819959	-0.384211	1.232240	0.071247	0.585869	1.581004
3D asymptotic solutions			0.6455	1.1049	0.8200	-0.3842	1.232	0.0712	0.5859	1.581
3D solutions			0.6455	1.1049	0.8200	-0.3842	1.232	0.0712	0.5859	1.581

Table 3: The elastic and electric field variables at crucial positions of single-layer piezoelectric hollow cylinders under electric potential (Case 2 with $\hat{m}=1$, $\hat{n}=0$ and $R/2h$=4)

n	a	Theories	-$\bar{u}\left(0,-h\right)$	-$\bar{w}\left(\frac{L}{2},-h\right)$	-$\bar{D}_z\left(\frac{L}{2},-h\right)$	-$\bar{\sigma}_x\left(\frac{L}{2},-h\right)$	-$\bar{\sigma}_\theta\left(\frac{L}{2},-h\right)$	-$\bar{\tau}_{xz}\left(0,0\right)$	-$\bar{\sigma}_z\left(\frac{L}{2},0\right)$	-$\bar{\varphi}\left(\frac{L}{2},0\right)$
2	2.1Δz	Present *NP*= 7	0.045387	-0.887152	-68.0313	0.123805	-0.554607	-0.216635	-0.123977	0.527296
		NP= 9	0.045628	-0.886683	-68.0302	0.123737	-0.552526	-0.214098	-0.123352	0.529272
		NP=11	0.045761	-0.886394	-68.0268	0.123681	-0.551382	-0.216017	-0.123739	0.528114
		NP=21	0.045964	-0.885936	-68.0202	0.123581	-0.549639	-0.215640	-0.123695	0.528493
3	3.1Δz	Present *NP*= 7	0.046051	-0.885739	-68.0174	0.123540	-0.548889	-0.215820	-0.123833	0.528436
		NP= 9	0.046045	-0.885752	-68.0175	0.123540	-0.548944	-0.215725	-0.123724	0.528460
		NP=11	0.046044	-0.885756	-68.0175	0.123541	-0.548960	-0.215777	-0.123764	0.528446
		NP=21	0.046042	-0.885758	-68.0175	0.123541	-0.548971	-0.215764	-0.123752	0.528449
4	4.1Δz	Present *NP*= 7	0.046055	-0.885733	-68.0174	0.123539	-0.548859	-0.215782	-0.123763	0.528446
		NP= 9	0.046047	-0.885748	-68.0175	0.123541	-0.548927	-0.215761	-0.123754	0.528451
		NP=11	0.046045	-0.885754	-68.0175	0.123541	-0.548951	-0.215768	-0.123755	0.528449
		NP=21	0.046042	-0.885758	-68.0175	0.123541	-0.548970	-0.215765	-0.123753	0.528449
3D asymptotic solutions			0.0460	-0.8858	-68.02	0.1235	-0.5490	-0.2158	-0.1238	0.528
3D solutions			0.0460	-0.8858	-68.02	0.1235	-0.5490	-0.2158	-0.1238	0.528

Table 4: The elastic and electric field variables at crucial positions of multilayered hybrid piezoelectric hollow cylinders under mechanical load (Case 1 with $R/2h$=5, L/R=4, n=3, $a = 3.1\Delta z$)

z	*Theories*	$\bar{v}\left(\frac{L}{2},\frac{\pi}{8},z\right)$	$\bar{w}\left(\frac{L}{2},0,z\right)$	$\bar{\sigma}_\theta\left(\frac{L}{2},0,z\right)$	$\bar{\tau}_{x\theta}\left(0,\frac{\pi}{8},z\right)$	$\bar{\tau}_{\theta z}\left(\frac{L}{2},\frac{\pi}{8},z\right)$	$\bar{\sigma}_z\left(\frac{L}{2},0,z\right)$	$\bar{\varphi}\left(\frac{L}{2},0,z\right)$	$\bar{D}_z\left(\frac{L}{2},0,z\right)$
h	Present N_p=7	-1.3745e-11	1.2580e-09	24.8111	2.3350	0.0000	1.0000	0.0000	-1.7230e-11
	$N_p = 9$	-1.3749e-11	1.2580e-09	24.8101	2.3349	0.0000	1.0000	0.0000	-1.7231e-11
	3D asymptotic sol.	-1.3750 e-11	1.2579e-09	24.8090	2.3349	0.0000	1.0000	0.0000	-1.7236 e-11
$0.9h^+$	Present N_p=7	-5.8707e-11	1.2632e-09	21.3902	1.9219	-0.8685	7.8032e-01	1.1619e-02	-2.2569e-11
	$N_p = 9$	-5.8709e-11	1.2631e-09	21.3892	1.9218	-0.8685	7.8032e-01	1.1618e-02	-2.2570e-11
	3D asymptotic sol.	-5.8709 e-11	1.2631e-09	21.3880	1.9218	-0.8685	7.8033e-01	1.1617e-02	-2.2575e-11
$0.3h^+$	Present N_p=7	-2.1769e-10	1.2615e-09	0.9608	0.0357	-1.3683	4.5430e-01	1.1472e-02	8.3899e-12
	$N_p = 9$	-2.1768e-10	1.2615e-09	0.9607	0.0357	-1.3683	4.5429e-01	1.1471e-02	8.3877e-12
	3D asymptotic sol.	-2.1768e-10	1.2615e-09	0.9606	0.0357	-1.3682	4.5430e-01	1.1471e-02	8.3808e-12
0	Present N_p=7	-3.1802e-10	1.2611e-09	-0.3705	-0.1269	-2.2655	2.5063e-02	1.1639e-02	2.6008e-11
	$N_p = 9$	-3.1801e-10	1.2611e-09	-0.3704	-0.1269	-2.2655	2.5111e-02	1.1638e-02	2.6005e-11
	3D asymptotic sol.	-3.1800e-10	1.2611e-09	-0.3704	-0.1268	-2.2654	2.5134e-02	1.1638e-02	2.5996e-11
$-0.3h^+$	Present N_p=7	-4.1826e-10	1.2595e-09	-15.4866	-0.2930	-1.4486	3.6482e-03	1.1988e-02	4.5629e-11
	$N_p = 9$	-4.1826e-10	1.2594e-09	-15.4878	-0.2930	-1.4484	3.7277e-03	1.1988e-02	4.5625e-11
	3D asymptotic sol.	-4.1824e-10	1.2594e-09	-15.4880	-0.2930	-1.4483	3.7437e-03	1.1987e-02	4.5616e-11
$-0.9h^+$	Present N_p=7	-5.6560e-10	1.2481e-09	-2.4014	-0.7356	-1.1877	-2.6398e-01	1.3329e-02	9.3353e-11
	$N_p = 9$	-5.6557e-10	1.2480e-09	-2.4013	-0.7356	-1.1876	-2.6396e-01	1.3328e-02	9.3346e-11
	3D asymptotic sol.	-5.6555e-10	1.2480e-09	-2.4018	-0.7356	-1.1875	-2.6393e-01	1.3327e-02	9.3333e-11
$-h$	Present N_p=7	-6.1307e-10	1.2419e-09	-29.0426	-3.6325	0.0000	0.0000	0.0000	8.5719e-11
	$N_p = 9$	-6.1304e-10	1.2419e-09	-29.0410	-3.6323	0.0000	0.0000	0.0000	8.5713e-11
	3D asymptotic sol.	-6.1302e-10	1.2419e-09	-29.0390	-3.6322	0.0000	0.0000	0.0000	8.5701e-11

Table 5: The elastic and electric field variables at crucial positions of multilayered hybrid piezoelectric hollow cylinders under electric potential (Case 2 with $R/2h$=5, L/R=4, n=3, $a = 3.1\Delta z$)

z	*Theories*	$\bar{v}\left(\frac{L}{2},\frac{\pi}{8},z\right)$	$\bar{w}\left(\frac{L}{2},0,z\right)$	$\bar{\sigma}_\theta\left(\frac{L}{2},0,z\right)$	$\bar{\tau}_{x\theta}\left(0,\frac{\pi}{8},z\right)$	$\bar{\tau}_{\theta z}\left(\frac{L}{2},\frac{\pi}{8},z\right)$	$\bar{\sigma}_z\left(\frac{L}{2},0,z\right)$	$\bar{\varphi}\left(\frac{L}{2},0,z\right)$	$\bar{D}_z\left(\frac{L}{2},0,z\right)$
h	Present N_p=7	8.7324e-11	1.7225e-11	-11.2038	0.9998	0.0000	0.0000	1.0000	-1.6837e-08
	$N_p = 9$	8.7324e-11	1.7228e-11	-11.2037	0.9998	0.0000	0.0000	1.0000	-1.6837e-08
	3D asymptotic sol.	8.7323 e-11	1.7236e-11	-11.2040	0.9998	0.0000	0.0000	1.0000	-1.6837 e-08
$0.9h^+$	Present N_p=7	6.7783e-11	2.6915e-11	-12.0471	0.8204	0.4212	1.1455e-01	0.9418	-1.6460e-08
	$N_p = 9$	6.7782e-11	2.6917e-11	-12.0471	0.8204	0.4212	1.1455e-01	0.9418	-1.6460e-08
	3D asymptotic sol.	6.7781 e-11	2.6925e-11	-12.0470	0.8204	0.4212	1.1455e-01	0.9418	-1.6460e-08
$0.3h^+$	Present N_p=7	1.9084e-11	2.7163e-11	0.2793	0.1251	0.3568	1.8709e-01	0.6322	-1.5219e-08
	$N_p = 9$	1.9084e-11	2.7166e-11	0.2794	0.1251	0.3568	1.8709e-01	0.6322	-1.5219e-08
	3D asymptotic sol.	1.9082e-11	2.7173e-11	0.2792	0.1251	0.3568	1.8709e-01	0.6322	-1.5219e-08
0	Present N_p=7	1.1996e-11	2.6271e-11	2.7522	0.1137	-0.0086	1.1843e-01	0.4850	-1.4835e-08
	$N_p = 9$	1.1995e-11	2.6273e-11	2.7521	0.1137	-0.0086	1.1843e-01	0.4850	-1.4835e-08
	3D asymptotic sol.	1.1992e-11	2.6283e-11	2.7521	0.1137	-0.0086	1.1842e-01	0.4850	-1.4835e-08
$-0.3h^+$	Present N_p=7	1.2146e-11	2.6306e-11	2.8212	0.1153	-0.3507	1.6688e-02	0.3407	-1.4637e-08
	$N_p = 9$	1.2146e-11	2.6309e-11	2.8213	0.1153	-0.3508	1.6681e-02	0.3407	-1.4637e-08
	3D asymptotic sol.	1.2142e-11	2.6319e-11	2.8213	0.1153	-0.3508	1.6682e-02	0.3407	-1.4637e-08
$-0.9h^+$	Present N_p=7	4.6154e-11	3.0752e-11	0.4595	0.1638	-0.4883	-1.1300e-01	0.0527	-1.4906e-08
	$N_p = 9$	4.6152e-11	3.0755e-11	0.4594	0.1638	-0.4883	-1.1300e-01	0.0527	-1.4906e-08
	3D asymptotic sol.	4.6147e-11	3.0749e-11	0.4597	0.1638	-0.4884	-1.1301e-01	0.0527	-1.4906e-08
$-h$	Present N_p=7	4.4008e-11	3.9321e-11	-11.3254	0.6861	0.0000	0.0000	0.0000	-1.5057e-08
	$N_p = 9$	4.4006e-11	3.9324e-11	-11.3255	0.6861	0.0000	0.0000	0.0000	-1.5057e-08
	3D asymptotic sol.	4.4001e-11	3.9317e-11	-11.3260	0.6860	0.0000	0.0000	0.0000	-1.5057e-08

6.2 Multilayered piezoelectric hollow cylinders

A coupled analysis of multilayered piezoelectric hollow cylinders with closed-circuit surface conditions and subject to a nonaxisymmetric mechanical load ($\bar{q}_3^+ = q_0 \sin(\pi x_1/L)\cos 4x_2$, $q_0 = -1\mathrm{N/m^2}$) and electric potential ($\Phi^+ = \varphi_0 \sin(\pi x_1/L)\cos 4x_2$, $\varphi_0 = 1\mathrm{V}$) on the outer surface of the cylinder is considered in Tables 4 and 5, respectively. The cylinder is composed of a $[0^0/90^0/0^0]$ laminated composite cylinder bonded with piezoelectric layers of PZT-4 on the outer and inner surfaces (see Fig. 1). The thickness ratio of each layer is PZT-4 layer : 0^0-layer : 90^0-layer : 0^0-layer : PZT-4 layer = $0.1h$: $0.6h$: $0.6h$: $0.6h$: $0.1h$. The geometric parameters are taken as $R/2h$=5 and L/R=4. The material properties of the composite material (Graphite/Epoxy) and piezoelectric material (PZT-4) are given in Table 1. A set of normalized variables is defined as follows:

In the cases of applied mechanical loads,

$$(\bar{u},\bar{w}) = (u_1 c^*/q_0(2h), u_3 c^*/q_0(2h)),$$

$$(\bar{\sigma}_x,\bar{\sigma}_\theta,\bar{\tau}_{x\theta},\bar{\sigma}_z,\bar{\tau}_{xz}) = (\sigma_1,\sigma_2,\tau_{12},\sigma_3,\tau_{13})/q_0,$$

$$(\bar{D}_x,\bar{D}_z) = (D_1 c^*/q_0 e^*, D_3 c^*/q_0 e^*), \quad \bar{\varphi} = \Phi e^*/q_0(2h). \tag{57}$$

where $c^* = 1\mathrm{N/m^2}$, $e^* = 1\mathrm{C/m^2}$.

In the cases of applied electrical potential,

$$(\bar{u},\bar{w}) = (u_1 c^*/\varphi_0 e^*, u_3 c^*/\varphi_0 e^*),$$

$$(\bar{\sigma}_x,\bar{\sigma}_\theta,\bar{\tau}_{x\theta},\bar{\sigma}_z,\bar{\tau}_{xz}) = (\sigma_1,\sigma_2,\tau_{12},\sigma_3,\tau_{13})(2h/\varphi_0 e^*),$$

$$(\bar{D}_x,\bar{D}_z) = \left(2hD_1 c^*/\varphi_0 (e^*)^2, 2hD_3 c^*/\varphi_0 (e^*)^2\right), \quad \bar{\varphi} = \Phi/\varphi_0. \tag{58}$$

The values of elastic and electric field variables induced at the interfaces between adjacent layers, outer and inner surfaces, and the mid-surface of the hollow cylinder under the loading conditions of Cases 1 and 2 with $\hat{m} = 1$, $\hat{n} = 4$ are presented in Tables 4 and 5, respectively. In the present analysis, the values of n, a and N_p are taken as n=3, a=3.1$\Delta z^{(m)}$ and N_p=7, 9. The present solutions are compared with the 3D asymptotic solutions available in the literature (Wu, Syu and Lo, 2007), and Tables 4 and 5 show that they are in excellent agreement. In addition, in views of the inherent Kronecker delta properties of these DRK interpolation functions, it is also shown that the present analysis leads to the continuous values of the primary variables at the interfaces between adjacent layers, and the boundary conditions on the lateral surfaces are exactly satisfied.

6.3 Functionally graded piezoelectric hollow cylinders

A coupled analysis of FG piezoelectric hollow cylinders subjected to the loading conditions of Cases 1–4 on the lateral surfaces with $\hat{m} = 1$and $\hat{n} = 4$, is considered. The geometric parameters of the cylinders are $R/2h = 10$, $L/R = 4$. The dimensionless variables used in the cases of applied mechanical loads (Cases 1 and 3) and applied electric potential (Case 2) are identical to those used in Example 6.1 (i.e., (57)–(58)). The set of dimensionless variables in the cases of applied electric displacement is defined as

$$
\begin{aligned}
&(\bar{u}, \bar{w}) = \left(u_1 e^* / D_0 (2h), u_3 e^* / D_0 (2h)\right), \\
&(\bar{\sigma}_x, \bar{\sigma}_\theta, \bar{\tau}_{x\theta}, \bar{\sigma}_z, \bar{\tau}_{xz}) = (\sigma_1, \sigma_2, \tau_{12}, \sigma_3, \tau_{13}) e^* / D_0 c^*, \\
&(\bar{D}_x, \bar{D}_z) = (D_1/D_0, D_3/D_0), \\
&\bar{\varphi} = \Phi (e^*)^2 / D_0 c^* (2h).
\end{aligned} \tag{59}
$$

The material properties are assumed to obey the exponent-law dependence on the thickness coordinate of the cylinder and are given as (52), where the material-property gradient index κ is taken as κ=-3.0, -1.5, 0.0, 1.5, 3.0 and the material properties of bottom surface of the cylinder are considered to be the same as PZT-4, the material properties of which are given in Table 1. The through-thickness distributions of various variables in the elastic and electric fields induced in the cylinders under four different loading conditions (i.e., Cases 1–4) are presented in Figs. 2–5, respectively. It is shown in Figs. 2 and 4 that the through-thickness distributions of various elastic variables induced in the cylinder with closed-circuit surface conditions are almost identical to those induced in the cylinder with open-circuit surface conditions in the cases of applied mechanical loads, whereas the through-thickness distributions of electric variables induced in the cylinders with the closed-circuit and open-circuit surface conditions are largely different from each other. Figs. 2(a)–5(a) and 2(b)–5(b) show that the through-thickness distributions of the elastic displacements appear to be linear in both homogeneous cylinders (i.e., κ=0) and functionally graded cylinders ($\kappa \neq 0$). Figs. 2(c)–5(c) and 2(d)–5(d) show that the through-thickness distributions of the in-surface stresses appear to be linear in homogeneous cylinders, whereas these distributions become higher-degree polynomials in FG cylinders, and these dramatically change through the thickness coordinate when the absolute value of κ becomes larger. Figs. 2(e, f) and 4(e, f) show that the through-thickness distributions of the transverse shear and normal stresses appear to be parabolic functions in homogeneous cylinders. These distributions become higher-degree polynomials in FG cylinders. In addition, the magnitude of these stresses increases in the bottom half ($-1 \leq z \leq 0$) and decreases in the top half

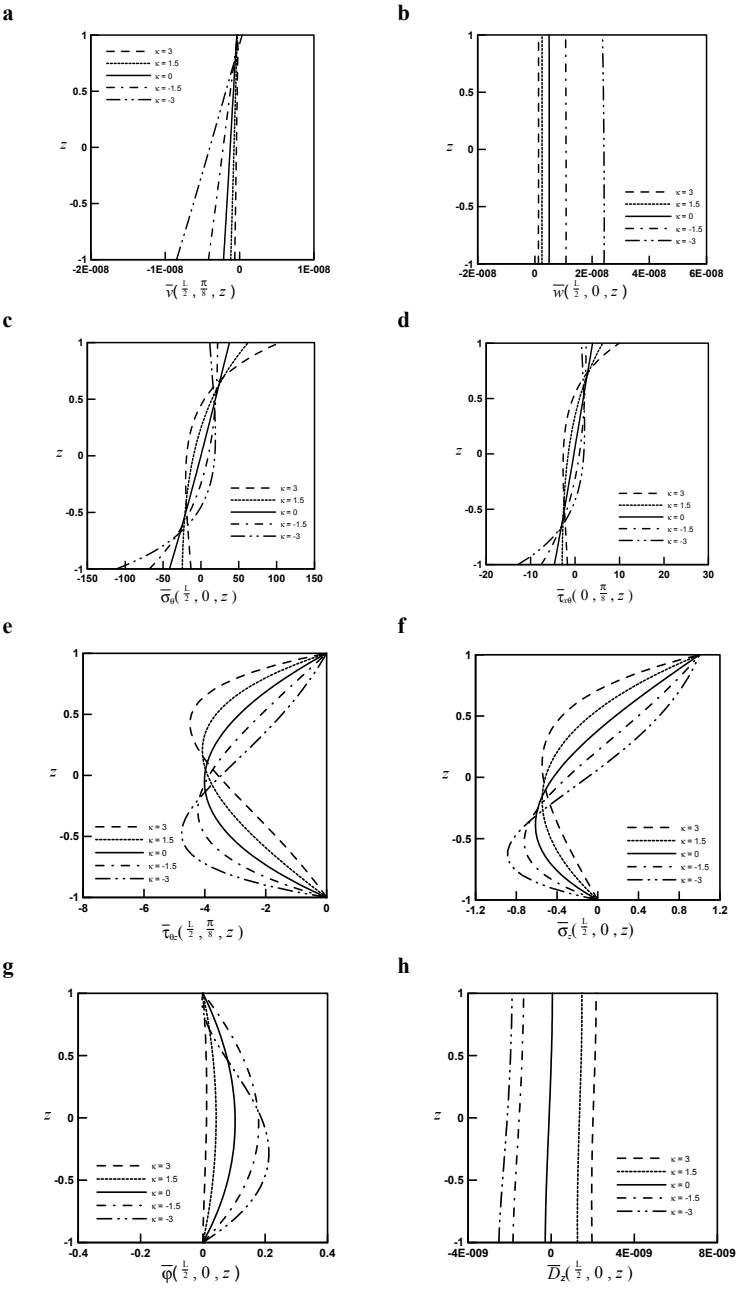

Figure 2: The through-thickness distributions of various field variables in an FG hollow cylinder with the surface conditions of Case 1.

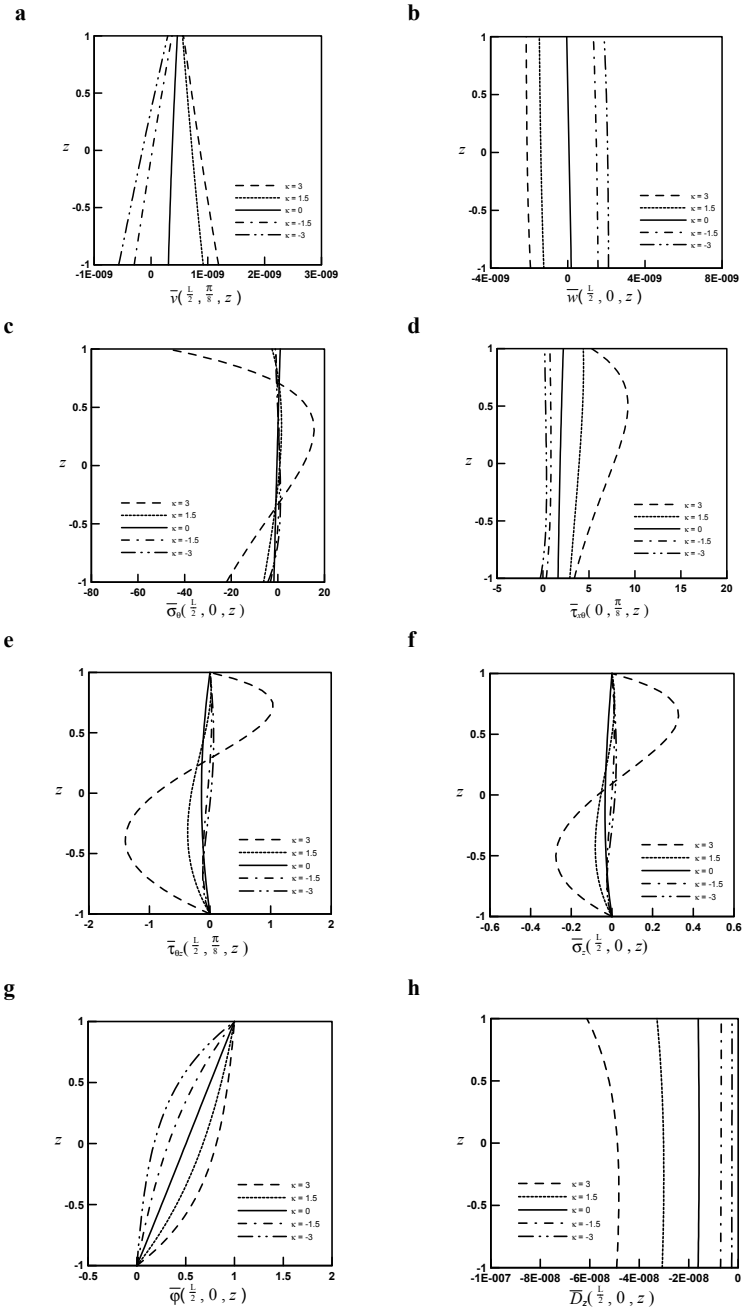

Figure 3: The through-thickness distributions of various field variables in an FG hollow cylinder with the surface conditions of Case 2.

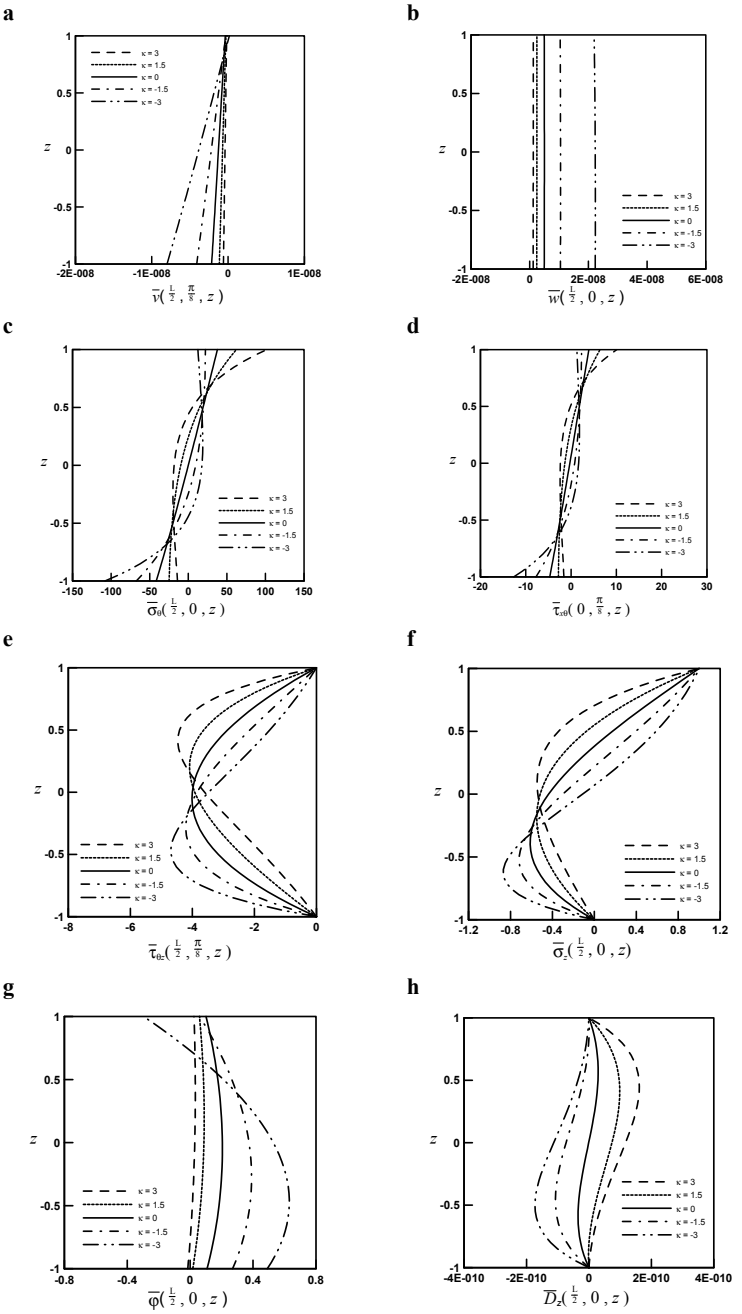

Figure 4: The through-thickness distributions of various field variables in an FG hollow cylinder with the surface conditions of Case 3.

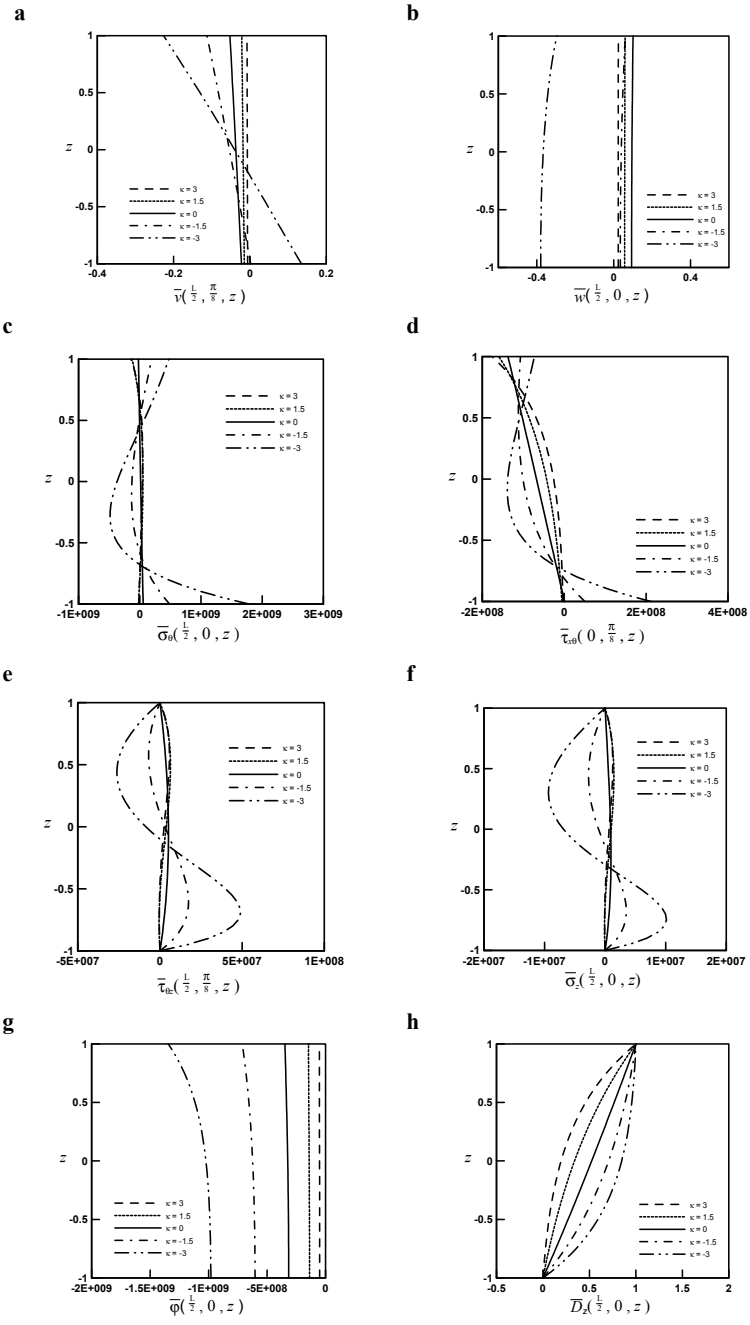

Figure 5: The through-thickness distributions of various field variables in an FG hollow cylinder with the surface conditions of Case 4.

($0 \leq z \leq 1$) of the cylinder when κ becomes a negative value, whereas it decreases in the bottom half and increases in the top half of the cylinder when κ becomes a positive value. Figs. 3(e, f) and 5(e, f) show that the through-thickness distributions of transverse shear and normal stresses appear to be higher-degree polynomials when the cylinders are subjected to the electric loads. These distributions change dramatically when the material-property gradient index κ becomes a positive value in Case 2, while they change dramatically when κ becomes a negative value in Case 4. Figs. 2–5 show that the distributions of elastic and electric variables through the thickness of FG cylinders reveal different patterns from the distributions with homogeneous cylinders, and the influence of the material-property gradient index κ on the field variables is significant. In addition, it is seen from Figs. 2(c, f, g, h)–5(c, f, g, h) that the prescribed boundary conditions on the lateral surfaces of the cylinder are exactly satisfied.

7 Concluding remarks

In this paper we have developed a meshfree collocation method based on the differential reproducing kernel interpolation for the three-dimensional static analysis of simply-supported, FG piezoelectric hollow cylinders with closed-circuit and open-circuit surface conditions. Four different lateral surface conditions of the cylinders, namely closed-circuit and applied mechanical load, closed-circuit and applied electric potential, open-circuit and applied mechanical load, and open-circuit and applied electric displacement, are considered. The accuracy and the rate of convergence of the present DRK interpolation-based collocation method are evaluated in comparison with the available 3D solutions and 3D asymptotic solutions, with which the present solutions are shown to converge rapidly and be in excellent agreement. It is noted that the distributions of elastic and electric variables through the thickness of FG cylinders reveal different patterns from those distributions of homogeneous cylinders, and the influence of the material-property gradient index κ on the field variables is significant.

Acknowledgement: This work was supported by the National Science Council of Republic of China through Grant NSC 97-2221-E006-128-MY3.

References

Akhras, G.; Li, W.C. (2007): Three-dimensional static, vibration and stability analysis of piezoelectric composite plates using a finite layer method. *Smart Materials and Structures*, vol. 16, pp. 561–569.

Aluru, N.R. (2000): A point collocation method based on reproducing kernel ap-

proximations. *International Journal for Numerical Methods in Engineering*, vol. 47, pp. 1083–1121.

Atluri, S.N. (2004): The Meshless Method (MLPG) for Domain & BIE Discritizations, Tech Science Press, USA.

Atluri, S.N.; Shen, S. (2002a): The meshless local Petrov-Galerkin (MLPG) method: A simple & less-costly alternative to the finite element and boundary element methods. *CMES: Computer Modeling in Engineering & Sciences*, vol. 3, pp. 11–51.

Atluri, S.N.; Shen, S. (2002b): The Meshless Local Petrov-Galerkin (MLPG) Method, Tech Science Press, USA.

Atluri, S.N.; Zhu, T. (1998): A new meshless local Petrov-Galerkin (MLPG) approach in computational mechanics. *Computational Mechanics*, vol. 22, pp. 117–127.

Atluri, S.N.; Zhu, T. (2000): New concepts in meshless methods. *International Journal of Numerical Methods in Engineering*, vol. 47, pp. 537–556.

Atluri, S.N.; Han, Z.D.; Rajendran, A.M. (2004): A new implementation of the meshless finite volume method, through the MLPG mixed approach. *CMES: Computer Modeling in Engineering & Sciences*, vol. 6, pp. 491–513.

Atluri, S.N.; Han, Z.D.; Shen, S. (2003): Meshless local Petrov-Galerkin (MLPG) approaches for solving the weakly-singular traction & displacement boundary integral equations. *CMES: Computer Modeling in Engineering & Sciences*, vol. 4, pp. 507–517.

Belytschko, T.; Lu, Y.Y.; Gu, L. (1994): Element-Free Galerkin Methods. *International Journal for Numerical Methods in Engineering*, vol. 37, pp. 229–256.

Belytschko, T.; Krongauz, Y.; Organ D.; Fleming, M.; Krysl, P. (1996): Meshless methods: An overview and recent developments. *Computer Methods in Applied Mechanics and Engineering*, vol. 139, pp. 3–47.

Chen, J.S.; Han, W.; You, Y.; X. Meng, X. (2003): A reproducing kernel method with nodal interpolation property. *International Journal for Numerical Methods in Engineering*, vol. 56, pp. 935–960.

Cheung, Y.K.; Jiang, C.P. (2001): Finite layer method in analyses of piezoelectric composite laminates. *Computer Methods in Applied Mechanics and Engineering*, vol. 191, pp. 879–901.

Heyliger, P. (1997a): A note on the static behavior of simply-supported laminated piezoelectric cylinders. *International Journal of Solids and Structures*, vol. 34, pp. 3781–3794.

Heyliger, P. (1997b): Exact solutions for simply supported laminated piezoelectric plates. *Journal of Applied Mechanics*, vol. 64, pp. 299–306.

Heyliger, P.; Brooks, S. (1996): Exact solutions for laminated piezoelectric plates in cylindrical bending. *Journal of Applied Mechanics*, vol. 63, pp. 903–910.

Heyliger, P.; Brooks, S. (1995): Free vibration of piezoelectric laminates in cylindrical bending. *International Journal of Solids and Structures*, vol. 32, pp. 2945–2960.

Huerta, A.; Fermandez-Mendez, S. (2000): Enrichment and coupling of the finite element and meshless methods. *International Journal for Numerical Methods in Engineering*, vol. 48, pp. 1615–1636.

Kapuria, S.; Dumir, P.C.; Sengupta, S. (1997): Nonaxisymmetric exact piezothermoelastic solution for laminated cylindrical shell. *AIAA Journal*, vol. 35, pp. 1792–1795.

Kapuria, S.; Sengupta, S.; Dumir, P.C. (1997a): Three-dimensional solution for simply-supported piezoelectric cylindrical shell for axisymmetric load. *Computer Methods in Applied Mechanics and Engineering*, vol. 140, pp. 139–155.

Kapuria, S.; Sengupta, S.; Dumir, P.C. (1997b): Three-dimensional solution for a hybrid cylindrical shell under axisymmetric thermoelectric load. *Archive of Applied Mechanics*, vol. 67, pp. 320–330.

Lancaster, P.; Salkauakas, K. (1981): Surfaces generated by moving least squares methods. *Mathematics of Computation*, vol. 37, pp. 141–158.

Liu G.R. (2003): Meshfree Methods Moving beyond the Finite Element Method. CRC Press, USA.

Liu, W.K.; Jun, S.; Zhang, Y.F. (1995): Reproducing kernel particle methods. *International Journal for Numerical Methods in Engineering*, vol. 20, pp. 1081–1106.

Nayroles, B.; Touzot, G.; Villon, P. (1992): Generalizing the finite element method: diffuse approximation and diffuse elements. *Computational Mechanics*, vol. 10, pp. 307–318.

Oñate, E.; Idelsohn, S.; Zienkiewicz, O.C.; Taylor, R.L. (1996): A finite point method in computational mechanics–Applications to convective transport and fluid flow. *International Journal for Numerical Methods in Engineering*, vol. 39, pp. 3839–3866.

Ramirez, F.; Heyliger, P.R.; Pan, E. (2006a): Static analysis of functionally graded elastic anisotropic plates using a discrete layer approach. *Composites Part B: Engineering*, vol. 37, pp. 10–20.

Ramirez, F.; Heyliger, P.R.; Pan, E. (2006b): Discrete layer solution to free vibration of functionally graded magneto-electro-elastic plates. *Mechanics of Advanced Materials and Structures*, vol. 13, pp. 249–266.

Sladek, J.; Sladek, V.; Krivacek, J.; Zhang, C.H. (2005): Meshless local Petrov-Galerkin method for stress and crack analysis in 3D axisymmetric FGM bodies. *CMES: Computer Modeling in Engineering & Sciences*, vol. 8, pp. 259–270.

Sladek, J.; Sladek, V.; Tan, C.L.; Atluri, S.N. (2008): Analysis of transient heat conduction in 3D anisotropic functionally graded solids. *CMES: Computer Modeling in Engineering & Sciences*, vol. 32, pp. 161–174.

Sladek, J.; Sladek, V.; Zhang, C.; Solek, P. (2007): Application of MLPG to thermo-piezoelectricity. *CMES: Computer Modeling in Engineering & Sciences*, vol. 22, pp. 217–234.

Sladek, J.; Sladek, V.; Zhang, C.; Garciasanche, F.; W'unsche, M. (2006): Meshless local Petrov-Galerkin method for plane piezoelectricity. *CMC: Computers, Materials, & Continua*, vol. 4, pp. 109–118.

Wu, C.P.; Chi, Y.W. (2004): A refined asymptotic theory for the nonlinear analysis of laminated cylindrical shells. *CMC: Computers, Materials, & Continua*, vol. 1, pp. 337–352.

Wu, C.P.; Liu, K.Y. (2007): A state space approach for the analysis of doubly curved functionally graded elastic and piezoelectric shells. *CMC: Computers, Materials, & Continua*, vol. 6, pp. 177–199.

Wu, C.P.; Lo, J.Y. (2006): An asymptotic theory for dynamic response of laminated piezoelectric shells. *Acta Mechanica*, vol. 183, pp. 177–208.

Wu, C.P.; Lu, Y.C. (2009): A modified Pagano method for the 3D dynamic responses of functionally graded magneto-electro-elastic plates. *Composite Structures*, vol. 90, pp. 363–372.

Wu, C.P.; Syu, Y.S. (2006): Asymptotic solutions for multilayered piezoelectric cylinders under electromechanical loads. *CMC: Computers, Materials, & Continua*, vol. 4, pp. 87–108.

Wu, C.P.; Syu, Y.S. (2007): Exact solutions of functionally graded piezoelectric shells under cylindrical bending. *International Journal of Solids and Structures*, vol. 44, pp. 6450–6472.

Wu, C.P.; Tsai, Y.H. (2009): Cylindrical bending vibration of functionally graded piezoelectric shells using the method of perturbation. *International Journal of Engineering Mathematics*, vol. 63, pp. 95–119.

Wu, C.P.; Chen, S.J.; Chiu, K.H. (2009): Three-dimensional static behavior of functionally graded magneto-electro-elastic plates using the method of modified Pagano method. *Mechanics Research Communications*, `doi:10.1016/j.mechrescom.2009.10.003`.

Wu, C.P.; Chiu, K.H.; Wang, Y.M. (2008a): A review on the three-dimensional

analytical approaches of multilayered and functionally graded piezoelectric plates and shells. *CMC: Computers, Materials, & Continua*, vol. 8, pp. 93–132.

Wu, C.P.; Chiu, K.H.; Wang, Y.M. (2008b): A differential reproducing kernel particle method for the analysis of multilayered elastic and piezoelectric plates. *CMES: Computer Modeling in Engineering & Sciences*, vol. 27, pp. 163–186.

Wu, C.P.; Chiu, K.H.; Wang, Y.M. (2008c): A mesh-free DRK-based collocation method for the coupled analysis of functionally graded magneto-electro-elastic shells and plates. *CMES: Computer Modeling in Engineering & Sciences*, vol. 35, pp. 181–214.

Wu, C.P.; Lo, J.Y.; Chao, J.K. (2005): A three-dimensional asymptotic theory of laminated piezoelectric shells. *CMC: Computers, Materials, & Continua*, vol. 2, pp. 119–137.

Wu, C.P.; Syu, Y.S.; Lo, J.Y. (2007): Three-dimensional solutions for multilayered piezoelectric hollow cylinders by an asymptotic approach. *International Journal of Mechanical Sciences*, vol. 49, pp. 669–689.

Zhong, Z.; Shang, E.T. (2003): Three-dimensional exact analysis of a simply supported functionally gradient piezoelectric plate. *International Journal of Solids and Structures*, vol. 40, pp. 5335–5352.

Zhong, Z.; Shang, E.T. (2005): Exact analysis of simply supported functionally graded piezothermoelectric plates. *Journal of Intelligent Material Systems and Structures*, vol. 16, pp. 643–651.

Appendix A

The relevant coefficients of k_{ij} in (15) are given by

$$\tilde{c}_{ij} = c_{ij}/Q, \quad \tilde{e}_{ij} = e_{ij}/e, \quad \tilde{\eta}_{ij} = \eta_{ij}Q/e^2;$$

$$Q_{ij} = c_{ij} - c_{i3}a_j - e_{3i}b_j \text{ (i, j=1, 2, 6)}, \tilde{Q}_{ij} = Q_{ij}/Q;$$
$$a_i = (c_{i3}\eta_{33} + e_{3i}e_{33})/\Delta, \quad b_i = (e_{33}c_{i3} - e_{3i}c_{33})/\Delta \text{ (i=1, 2), and } \Delta = c_{33}\eta_{33} + e_{33}^2;$$

$$\bar{c} = c_{33}/\Delta, \quad \bar{\eta} = \eta_{33}/\Delta, \quad \bar{e} = e_{33}/\Delta, \quad \gamma_\theta = 1 + (hz/R). \tag{60}$$

Appendix B

The coefficients $\bar{k}_{ij}$ in (48) are given by

$$\bar{k}_{15} = k_{15}, \quad \bar{k}_{17} = -\tilde{m}, \quad \bar{k}_{18} = -\tilde{m}(h\tilde{e}_{15}/R\tilde{c}_{55}),$$

$$\bar{k}_{22} = k_{22}, \quad \bar{k}_{26} = k_{26}, \quad \bar{k}_{27} = \tilde{n}\,(1/\gamma_\theta), \quad \bar{k}_{28} = \tilde{n}\,(h\tilde{e}_{24}/R\gamma_\theta\tilde{c}_{44}),$$

$$\bar{k}_{31} = -\tilde{m}\left(\tilde{Q}_{21}/\gamma_\theta\right), \quad \bar{k}_{32} = \tilde{n}\left(\tilde{Q}_{22}/\gamma_\theta^2\right), \quad \bar{k}_{33} = k_{33}, \quad \bar{k}_{34} = k_{34}, \quad \bar{k}_{37} = k_{37},$$

$$\bar{k}_{44} = k_{44}, \quad \bar{k}_{48} = -\tilde{m}^2\,(h/R)\left[\left(\tilde{e}_{15}^2/\tilde{c}_{55}\right) + \tilde{\eta}_{11}\right] - \tilde{n}^2\left(h/R\gamma_\theta^2\right)\left[\left(\tilde{e}_{24}^2/\tilde{c}_{44}\right) + \tilde{\eta}_{22}\right],$$

$$\bar{k}_{51} = \tilde{m}^2\tilde{Q}_{11} + \tilde{n}^2\left(\tilde{Q}_{66}/\gamma_\theta^2\right), \quad \bar{k}_{52} = -\tilde{m}\tilde{n}\left[\left(\tilde{Q}_{12} + \tilde{Q}_{66}\right)/\gamma_\theta\right],$$

$$\bar{k}_{53} = -\tilde{m}\,(a_1 h/R), \quad \bar{k}_{54} = -\tilde{m}\,(b_1 e/Q), \quad k_{57} = -\tilde{m}\left(\tilde{Q}_{12}/\gamma_\theta\right),$$

$$k_{61} = -\tilde{m}\tilde{n}\left[\left(\tilde{Q}_{21} + \tilde{Q}_{66}\right)/\gamma_\theta\right], \quad k_{62} = \tilde{m}^2\tilde{Q}_{66} + \tilde{n}^2\left(\tilde{Q}_{22}/\gamma_\theta^2\right), \quad k_{63} = \tilde{n}\,(a_2 h/R\gamma_\theta),$$

$$k_{64} = \tilde{n}\,(b_2 e/Q\gamma_\theta), \quad \bar{k}_{66} = k_{66}, \quad \bar{k}_{67} = \tilde{n}\left(\tilde{Q}_{22}/\gamma_\theta^2\right),$$

$$\bar{k}_{73} = k_{73}, \quad \bar{k}_{74} = k_{74}, \quad \bar{k}_{77} = k_{77}, \quad \bar{k}_{84} = k_{84}, \quad \bar{k}_{87} = k_{87}.$$